Mathematical modeling and vibration analysis of rotating functionally graded porous spacecraft systems reinforced by graphene nanoplatelets

Tian Yu Zhao[a], **Yu Xuan Wang**[a], **Long Chen**[c*]

[a] School of Science, Northeastern University, Shenyang, 110819, China

ABSTRACT

This paper investigates the theoretical modeling and coupled free vibration behaviors of a rotating double-bladed shaft assembly resting on elastic supports in a spacecraft system. According to the Kirchhoff plate theory and the Euler-Bernoulli beam theory, the theoretical model is established. The studied rotor is considered to be made of porous foam metal matrix and graphene nanoplatelet (GPL) reinforcement. Non-uniform distributions of porosity and graphene nanoplatelets (GPLs) are taken into account and lead to functionally graded (FG) structures. The effective material properties of the double-bladed shaft are varying along the radius and thickness direction of the shaft and blade, respectively. Moreover, the rule of mixture, the Halpin-Tsai model, and the open-cell scheme are used to determine its material properties. Considering the gyroscopic effect, the Lagrange equation is utilized to derive the coupled equations of motion. Then the traveling wave frequencies of the double-bladed shaft assembly is obtained by employing the assumed modes method and substructure modal synthesis method. A detailed parametric analysis is conducted to examine the effects of the rotating speed, GPL weight fraction, GPL distribution pattern, GPL length-to-thickness ratio, GPL length-to-width ratio, porosity coefficient, porosity distribution pattern, shaft length-to-radius ratio, blade length-to-thickness ratio, support stiffness and support location on the free vibration behaviors of the double-bladed shaft assembly.

Keywords: graphene nanoplatelets; porosity; double-bladed shaft assembly; free vibration; rotation.

* Corresponding author.

E-mail address: chenlong@mail.neu.edu.cn (C. L.)

1. Introduction

Rotating double-bladed shaft assemblies are extensively applied in many engineering fields, such as spacecraft, aeroengine, marine propulsion system, et al. Because the double-bladed shaft assemblies are usually under the poor working conditions, their failures occur frequently, where the vibration failure is the most common [1-4].

Fig. 1 Rotating double-bladed shaft assemblies in a spacecraft.

In theory, the blade should be modeled by elastic plate model. For rotating plates, their vibration behaviors have been given in many open literatures [5-9]. Yoo et al. [10] presented the vibration performance of a rotating rectangular plate attached to a rigid hub. Liu et al. [11] investigated the dynamic behaviors of rotating cantilever plates with fully covered active constrained layer damping. Hashemi et al. [12] developed a finite element formulation to study the nonlinear vibration of a rotating thick plate. Li et al.[13] carried out the free vibration characteristics of FG rectangular plates with large overall motions. By adopting the finite element method, Arumugam et al. [14] studied free and forced vibrations of variable thickness tapered composite plates with whirl motion. According to the Mindlin plate theory, Rostami et al. [15] presented an analytical investigation on vibration characteristics of a rotating plate with a stagger angle.

From above, it can be told that the rotating blade (plate) is generally taken as an individual structure or attached to a rigid shaft in previous studies. However, the elasticity of the shaft in a double-bladed shaft assembly cannot be ignored. So, it is quite necessary to carry out coupled theoretical model of double-bladed shaft structure.

High strength and light weight have been the development tendency for the rotating double-bladed shaft structure. Great mechanical performance nanocomposite, such as graphene reinforced material and the like, can be adopted to meet the above requirements. Since Rafiee et al. [16] experimentally found that GPLs were significantly better than carbon nanotube as additives at low content, FG-GPLRC (functionally graded graphene nanoplatelet reinforced composite) [17-22] has stimulated a surge of scientific interest. In addition, metal foams are well known as a new type of advanced material due to its low density and excellent energy absorption [23-25]. Although the internal pores can weak the material stiffness, GPL nanofillers can be added to enhance the stiffness and keep its light weight. Yang, Kitipornchai and their patterns [26-30] had carried out a prominent investigation on the vibration performance of GPL reinforced porous structures. Within the frame of an improved Donnell nonlinear shell theory, Wang et al. [31] investigated the nonlinear vibration of porous cylindrical shells reinforced with GPLs. According to a trigonometric shear deformation theory, Anirudh et al. [32] studied vibration behaviors of an FG porous curved beams reinforced by GPLs. Forced vibration characteristics of GPL reinforced porous shell is carried out by Mirjavadi et al. [33]. Narayan et al. [34] investigated the free vibration of a GPL reinforced porous curved beam with large amplitude motion. Asemi et al. [35] studied the free vibration of porous annular sector plates reinforced by GPLs. By employing an efficient polygonal finite element method, Nguyen et al. [36] studied the free vibration of FG porous plates reinforced by GPLs. Due to the great enhancement effect on structure performance, GPL reinforced porous nanocomposite has a broad application prospect in a rotating double-bladed shaft system.

To sum up, this paper aims to conduct the theoretical modelling and vibration analysis of a rotating double-bladed shaft assembly. Based on the Euler-Bernoulli beam theory and the Kirchhoff plate theory, the rotating double-bladed shaft assembly is established. The rotor is considered to be made of porous foam metal matrix and GPL reinforcement. And its coupled equations of motion are derived by employing the Lagrange equation and solved by the substructure modal synthesis method and assumed modes method. Special attention is given to the effects of the material and

structural parameters on free vibrations of the double-bladed shaft assembly. Those findings in this paper provide adequate support to help the double-bladed shaft structure achieve better mechanical performance.

2. Theoretical formulations

2.1 *Modeling*

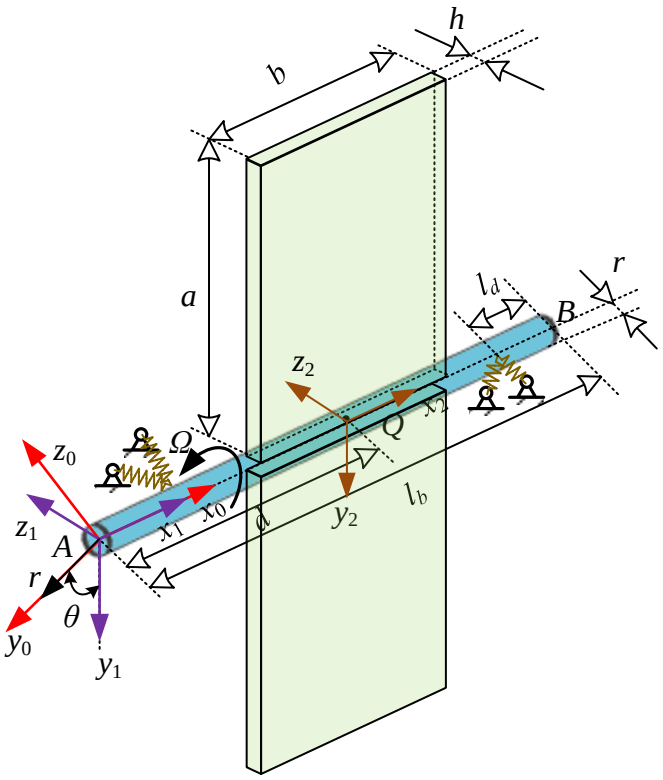

Fig. 1 A rotating double-bladed shaft resting on elastic supports.

As can be seen in Fig. 1, the coupled model of a rotating double-bladed shaft is established, where the blade and shaft are modeled by elastic plate model and elastic beam model, respectively. The dimensions of the two same rectangular thin plates are length a, width b and thickness h, while those of the circular-section beam are radius r_b and length l_b. The plates and beam are connected to at the midpoint Q of the plate width in which $AQ = d$. The two sets of elastic support with same stiffnesses k, are located at a distance of l_d from the ends (A, B) of the beam, respectively. The double-bladed shaft rotates at a constant speed Ω.

To describe the motion and deformation of the beam and plates, four coordinate systems

(A-$x_0y_0z_0$, A-$x_1r\theta$, A-$x_1y_1z_1$ and Q-$x_2y_2z_2$) are proposed as shown in Fig. 2, where A-$x_0y_0z_0$ is the fixed coordinate system; A-$x_1r\theta$ and A-$x_1y_1z_1$ are the rotating local coordinate systems for the beam; Q-$x_2y_2z_2$ is the rotating local coordinate system for the plates.

2.2 *Material property*

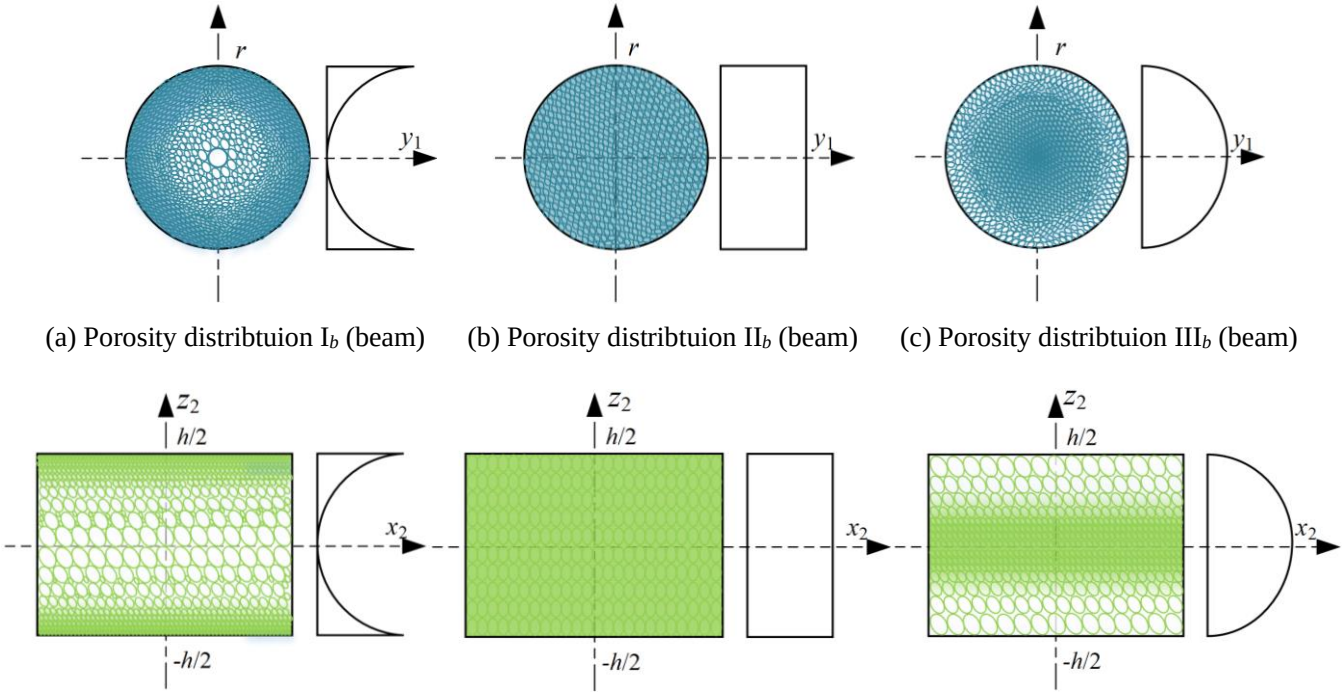

(a) Porosity distribtuion I_b (beam) (b) Porosity distribtuion II_b (beam) (c) Porosity distribtuion III_b (beam)

(d) Porosity distribtuion I_p (plate) (e) Porosity distribtuion II_p (plate) (f) Porosity distribtuion III_p (plate)

Fig. 2 Porosity distribution patterns of the beam and plate.

In this article, three porosity distribution patterns of the beam (I_b, II_b and III_b) and plate (I_p, II_p and III_p) are considered as shown in Fig. 2, where subscript b and p stand for the beam and plate, separately. Fig. 2 (a) and (d) plot positive parabolic porosity distributions of the beam and plate, separately, in this case more pores are setting around their surfaces. Fig. 2 (b) and (e) display uniform porosity distributions of the beam and plate, separately. Fig. 2 (c) and (f) show negative parabolic porosity distributions of the beam and plate, separately, in this case more pores are laying near their centers.

Based on the open-cell scheme [37], the effective material properties of the beam and plate are given by

$$
\text{beam}\begin{cases}
\text{Porosity I}_b: \begin{cases} E_b(z_2)=E_b^{*}(z_2)\left[1-e_b\cos(\pi z_2/h)\right] \\ \rho_b(z_2)=\rho_b^{*}(z_2)\left[1-e_{mb}\cos(\pi z_2/h)\right] \\ \mu_b(z_2)=\mu_b^{*}(z_2) \end{cases} \\
\text{Porosity II}_b: \begin{cases} E_b(z_2)=E_b^{*}(z_2)\alpha_b \\ \rho_b(z_2)=\rho_b^{*}(z_2)\alpha_{mb} \\ \mu_b(z_2)=\mu_b^{*}(z_2) \end{cases} \\
\text{Porosity III}_b: \begin{cases} E_b(z_2)=E_b^{*}(z_2)\left\{1-e_b^{*}\left[1-\cos(\pi z_2/h)\right]\right\} \\ \rho_b(z_2)=\rho_b^{*}(z_2)\left\{1-e_{mb}^{*}\left[1-\cos(\pi z_2/h)\right]\right\} \\ \mu_b(z_2)=\mu_b^{*}(z_2) \end{cases}
\end{cases} \tag{1}
$$

$$
\text{plate}\begin{cases}
\text{Porosity I}_p: \begin{cases} E_p(r)=E_p^{*}(r)\left[1-e_p\cos(\pi r/2r_b)\right] \\ \rho_p(r)=\rho_p^{*}(r)\left[1-e_{mp}\cos(\pi r/2r_b)\right] \\ \mu_p(r)=\mu_p^{*}(r) \end{cases} \\
\text{Porosity II}_p: \begin{cases} E_p(r)=E_p^{*}(r)\alpha_p \\ \rho_p(r)=\rho_p^{*}(r)\alpha_{mp} \\ \mu_p(r)=\mu_p^{*}(r) \end{cases} \\
\text{Porosity III}_p: \begin{cases} E_p(r)=E_p^{*}(r)\left\{1-e_p^{*}\left[1-\cos(\pi r/2r_b)\right]\right\} \\ \rho_p(r)=\rho_p^{*}(r)\left\{1-e_{mp}^{*}\left[1-\cos(\pi r/2r_b)\right]\right\} \\ \mu_p(r)=\mu_p^{*}(r) \end{cases}
\end{cases} \tag{2}
$$

where (e_{mb}, α_{mb}, e_{mb}^{*}) and (e_{mp}, α_{mp}, e_{mp}^{*}) are mass density coefficients of the beam and plate, separately; (e_b, α_b, e_b^{*}) and (e_p, α_p, e_p^{*}) are porosity coefficients of the beam and plate, separately.

According to the typical mechanical properties of metal foam

$$
\begin{cases}
\dfrac{E_b(z_2)}{E_b^{*}}=\left[\dfrac{\rho_b(z_2)}{\rho_b^{*}}\right]^2 \\
\dfrac{E_p(r)}{E_p^{*}}=\left[\dfrac{\rho_p(r)}{\rho_p^{*}}\right]^2
\end{cases} \tag{3}
$$

the porosity coefficients and mass density coefficients are related by

$$\begin{cases} 1-e_{mb}\cos\left(\pi z_2/h\right)=\sqrt{1-e_b\cos\left(\pi z_2/h\right)} \\ 1-e_{mb}^{\ *}\left[1-\cos\left(\pi z_2/h\right)\right]=\sqrt{1-e_b^{\ *}\left[1-\cos\left(\pi z_2/h\right)\right]} \\ \alpha_{mb}=\sqrt{\alpha_b} \end{cases} \tag{4}$$

$$\begin{cases} 1-e_{mp}\cos\left(\pi r/2r_b\right)=\sqrt{1-e_p\cos\left(\pi r/2r_b\right)} \\ 1-e_{mp}^{\ *}\left[1-\cos\left(\pi r/2r_b\right)\right]=\sqrt{1-e_p^{\ *}\left[1-\cos\left(\pi r/2r_b\right)\right]} \\ \alpha_{mp}=\sqrt{\alpha_p} \end{cases} \tag{5}$$

Due to equal quality for different distributions, one can obtained

$$\begin{cases} \int_0^{h/2}\sqrt{1-e_b\cos\left(\pi z_2/h\right)}\mathrm{d}z_2=\int_0^{h/2}\sqrt{\alpha_b}\mathrm{d}z_2=\int_0^{h/2}\sqrt{1-e_b^{\ *}\left[1-\cos\left(\pi z_2/h\right)\right]}\mathrm{d}z_2 \\ \int_0^{r_b}\sqrt{1-e_p\cos\left(\pi r/2r_b\right)}\mathrm{d}r=\int_0^{r_b}\sqrt{\alpha_p}\mathrm{d}r=\int_0^{r_b}\sqrt{1-e_b^{\ *}\left[1-\cos\left(\pi r/2r_b\right)\right]}\mathrm{d}r \end{cases} \tag{6}$$

Thus, it can be told that e_b and e_p can be given to determine all the porosity coefficients and mass density coefficients based on Eqs. (4-6).

Moreover, on the basis of the rule of mixture and the Halpin-Tsai model [38], Poisson's ratio (μ_b^*, μ_p^*), mass density (ρ_b^*, ρ_p^*) and Young's modulus (E_b^*, E_p^*) of the GPL reinforced structures without pores can be written as

$$\begin{cases} E_b^{\ *}=\dfrac{3}{8}\left(\dfrac{1+\dfrac{E_{gpl}-E_m}{E_{gpl}+\xi_{lb}E_m}\xi_{lb}V_{gplb}}{1-\dfrac{E_{gpl}-E_m}{E_{gpl}+\xi_{lb}E_m}V_{gplb}}\right)E_m+\dfrac{5}{8}\left(\dfrac{1+\dfrac{E_{gpl}-E_m}{E_{gpl}+\xi_{\kappa b}E_m}\xi_{\kappa b}V_{gplb}}{1-\dfrac{E_{gpl}-E_m}{E_{gpl}+\xi_{\kappa b}E_m}V_{gplb}}\right)E_m \\ \rho_b^{\ *}=\rho_{gpl}V_{gplb}+\rho_m\left(1-V_{gplb}\right) \\ \mu_b^{\ *}=\mu_{gpl}V_{gplb}+\mu_m\left(1-V_{gplb}\right) \end{cases} \tag{7}$$

$$\begin{cases} E_p^{\ *}=\dfrac{3}{8}\left(\dfrac{1+\dfrac{E_{gpl}-E_m}{E_{gpl}+\xi_{lp}E_m}\xi_{lp}V_{gplp}}{1-\dfrac{E_{gpl}-E_m}{E_{gpl}+\xi_{lp}E_m}V_{gplp}}\right)E_m+\dfrac{5}{8}\left(\dfrac{1+\dfrac{E_{gpl}-E_m}{E_{gpl}+\xi_{\kappa p}E_m}\xi_{\kappa p}V_{gplp}}{1-\dfrac{E_{gpl}-E_m}{E_{gpl}+\xi_{\kappa p}E_m}V_{gplp}}\right)E_m \\ \rho_p^{\ *}=\rho_{gpl}V_{gplp}+\rho_m\left(1-V_{gplp}\right) \\ \mu_p^{\ *}=\mu_{gpl}V_{gplp}+\mu_m\left(1-V_{gplp}\right) \end{cases} \tag{8}$$

in which subscript *gpl* and *m* represent the GPL and matrix, separately; (μ_{gpl}, μ_m), (ρ_{gpl}, ρ_m) and (E_{gpl}, E_m) are Poisson's ratio, mass density and Young's modulus of the GPL and matrix, separately.

To characterize the dimension and geometry of GPLs in the beam and plate, (ξ_{lb}, $\xi_{\kappa b}$) and (ξ_{lp}, $\xi_{\kappa p}$) are given by

$$\begin{cases} \xi_{lb} = \dfrac{2l_b}{t_b} \\ \xi_{\kappa b} = \dfrac{2\kappa_b}{t_b} \end{cases} \tag{9}$$

$$\begin{cases} \xi_{lp} = \dfrac{2l_p}{t_p} \\ \xi_{\kappa p} = \dfrac{2\kappa_p}{t_p} \end{cases} \tag{10}$$

where (t_b, κ_b l_b,) and (t_p, κ_p, l_p) are the average thickness, width and length of GPLs in the beam and plates, separately.

The GPL volume fractions of the beam (V_{gplb}) and plate (V_{gplb}) can be expressed as

$$\begin{cases} V_{gplb} = \dfrac{W_{gplb}}{W_{gplb} + \rho_{gpl}\left(1 - W_{gplb}\right)/\rho_m} \\ V_{gplp} = \dfrac{W_{gplp}}{W_{gplp} + \rho_{gpl}\left(1 - W_{gplp}\right)/\rho_m} \end{cases} \tag{11}$$

in which W_{gplb} and W_{gplp} are the GPL weight fractions of the beam and plate, separately.

In this text, three different GPL distribution patterns of the beam (X_b, U_b and O_b) and plate (X_p, U_p and O_p) are taken into consideration, separately. Fig. 3 (a, d) display the positive parabolic GPL distributions of the beam and plate, separately, where the GPL weight fractions are maximum around the surfaces of the beam and plate; Fig. 3 (b, e) plot the uniform GPL distributions of the beam and plate, where the GPL weight fractions remain constant; Fig. 3 (c, f) show the negative parabolic GPL distributions of the beam and plate, separately, where the GPL weight fractions are maximum in the center of the beam and plate.

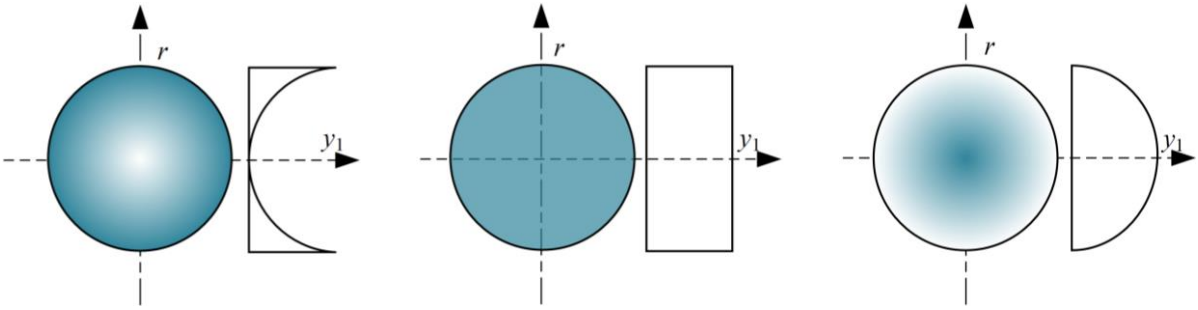

(a) GPL distribtuion X_b (beam) (b) GPL distribtuion U_b (beam) (c) GPL distribtuion O_b (beam)

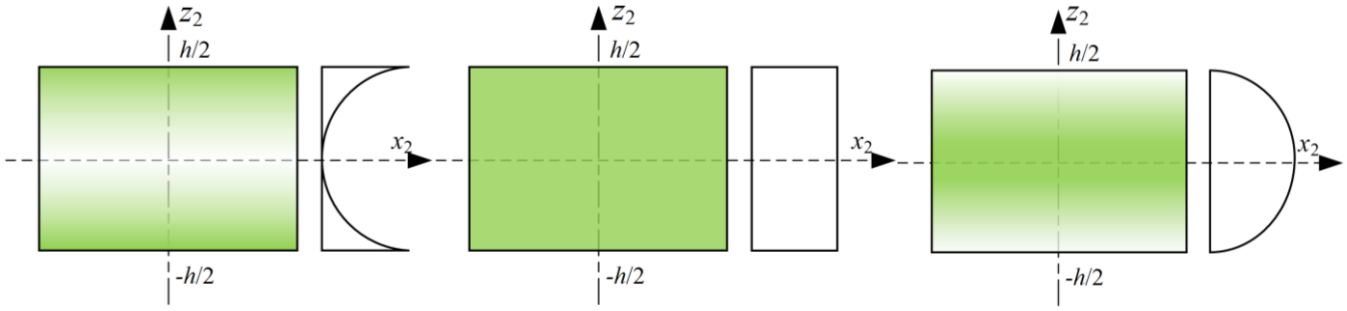

(d) GPL distribtuion X_p (plate) (e) GPL distribtuion U_p (plate) (f) GPL distribtuion O_p (plate)

Fig. 3 GPL distribution patterns of the beam and plate.

Thus, the expressions of GPL weight fractions corresponding to the present GPL distributions are given by

$$W_{gplb}(r)=\begin{cases}\dfrac{r^2}{r_b^{\,2}}\lambda_1 W_0 & \text{Pattern X}_b\\ \lambda_2 W_0 & \text{Pattern U}_b\\ \left(1-\dfrac{r^2}{r_b^{\,2}}\right)\lambda_3 W_0 & \text{Pattern O}_b\end{cases} \tag{12}$$

$$W_{gplp}(z_2)=\begin{cases}\dfrac{4z_2^{\,2}}{h^2}\lambda_4 W_0 & \text{Pattern X}_p\\ \lambda_5 W_0 & \text{Pattern U}_p\\ \left(1-\dfrac{4z_2^{\,2}}{h^2}\right)\lambda_6 W_0 & \text{Pattern O}_p\end{cases} \tag{13}$$

in which W_0 is the GPL characteristic value; (λ_1, λ_2, λ_3) and (λ_4, λ_5, λ_6) are the GPL weight fraction indices of the beam and plate, separately. They are determined by the total content of GPLs in the beam (W_{gplb}^{T}) and plate (W_{gplp}^{T}), separately.

2.3 *Energy function*

An arbitrary point M_1 in the beam is considered and its position vector can be written as

$$\mathbf{r}_{AM_1} = \left(v_b\theta_\eta - w_b\theta_\xi\right)\mathbf{i}_1 + \left(v_b\right)\mathbf{j}_1 + \left(w_b\right)\mathbf{k}_1 \tag{14}$$

where $\mathbf{i}_1$, $\mathbf{j}_1$ and $\mathbf{k}_1$ are the basis vectors of the coordinate system A-$x_1y_1z_1$; v_b and w_b are the beam displacements along y_1-axis and z_1-axis direction, respectively; θ_η and θ_ξ are the deflection angles caused by v_b and w_b, respectively, expressed as

$$\begin{cases} \theta_\eta = \dfrac{\partial v_b}{\partial x_1} \\ \theta_\xi = -\dfrac{\partial w_b}{\partial x_1} \end{cases} \tag{15}$$

The revolving speed of the local coordinate system A-$x_1y_1z_1$ with respect to the fixed coordinate system A-$x_0y_0z_0$ is

$$\boldsymbol{\varpi}_1 = \left(\Omega - \frac{\Omega}{2}\theta_\eta^2 - \frac{\Omega}{2}\theta_\xi^2 + \theta_\eta\dot{\theta}_\xi\right)\mathbf{i}_1 + \left(\dot{\theta}_\xi - \Omega\theta_\eta\right)\mathbf{j}_1 + \left(\dot{\theta}_\eta + \Omega\theta_\xi\right)\mathbf{k}_1 \tag{16}$$

Thus, the absolute velocity of the arbitrary point M_1 can be determined by

$$\begin{aligned} \dot{\mathbf{r}}_{AM_1} &= \mathrm{d}\mathbf{r}_{AM_1}/\mathrm{d}t + \boldsymbol{\varpi}_1 \times \mathbf{r}_{AM_1} \\ &= \left(\theta_\eta\dot{v}_b - \theta_\xi\dot{w}_b - \Omega\theta_\eta w_b - \Omega\theta_\xi v_b\right)\mathbf{i}_1 + \left(\dot{v}_b - \Omega w_b\right)\mathbf{j}_1 + \left(\dot{w}_b + \Omega v_b\right)\mathbf{k}_1 \end{aligned} \tag{17}$$

The kinetic energy of the beam can be obtained as

$$\begin{aligned} T_b &= \frac{1}{2}\int_0^{l_b}\int_0^{2\pi}\int_0^{r_b}\rho_b\dot{\mathbf{r}}_{AM_1}^{\mathrm{T}}\dot{\mathbf{r}}_{AM_1} r\mathrm{d}r\mathrm{d}\theta\mathrm{d}x_1 \\ &= \pi\int_0^{r_b}\int_0^{l_b}\rho_b r\left[\dot{v}_b^{\,2} + \dot{w}_b^{\,2} + 2\Omega\left(\dot{w}_b v_b - w_b\dot{v}_b\right) + \Omega^2\left(v_b^{\,2} + w_b^{\,2}\right)\right]\mathrm{d}x_1\mathrm{d}r \\ &\quad + \frac{\pi}{2}\int_0^{r_b}\int_0^{l_b}\rho_b r^3\left[\dot{\theta}_\xi^{\,2} + \dot{\theta}_\eta^{\,2} + 2\Omega\left(\dot{\theta}_\xi\theta_\eta + \theta_\xi\dot{\theta}_\eta\right) - \Omega^2\left(\theta_\xi^{\,2} + \theta_\eta^{\,2}\right)\right]\mathrm{d}x_1\mathrm{d}r \end{aligned} \tag{18}$$

Based on the Euler-Bernoulli beam theory, the deformation potential energy of the beam is

$$U_b = \frac{\pi}{2}\int_0^{r_b}\int_0^{l_b}\frac{E_b r^3}{1-\mu_b^{\,2}}\left[\left(\frac{\partial^2 v_b}{\partial x_1^{\,2}}\right)^2 + \left(\frac{\partial^2 w_b}{\partial x_1^{\,2}}\right)^2\right]\mathrm{d}x_1\mathrm{d}r \tag{19}$$

In this paper, the double plates are connected to the beam along their width directions. Because the beam is clamped by two plates, the vibration difference of the beam at connection position is

small. Therefore, the effect of the beam on the plates is simplified to be reflected by the displacements of connection midpoint Q.

An arbitrary point M_2 in the plate is taken into account and its position vector is

$$\mathbf{r}_{AM_2}=\mathbf{r}_{AQ}+\mathbf{r}_{QM_2}=\left(v_0\theta_{b\eta}-w_0\theta_{b\xi}-d\right)\mathbf{i}_2+\left(v_0\right)\mathbf{j}_2+\left(w_0+w_p\right)\mathbf{k}_2 \tag{20}$$

where $\mathbf{i}_2$, $\mathbf{j}_2$ and $\mathbf{k}_2$ are the basis vectors of the coordinate system Q-$x_2y_2z_2$; w_p is the plate displacement along z_2-axis direction; (v_0, w_0) and ($\theta_{b\eta}$, $\theta_{b\xi}$) are the displacements and deflection angles of the connection point Q in the beam, given by

$$\begin{cases} v_0=v_b\big|_{x_1=d} \\ w_0=w_b\big|_{x_1=d} \end{cases},\quad \begin{cases} \theta_{b\eta}=\dfrac{\partial v_b}{\partial x_1}\Big|_{x_1=d} \\ \theta_{b\xi}=-\dfrac{\partial w_b}{\partial x_1}\Big|_{x_1=d} \end{cases} \tag{21}$$

The revolving speed of the local coordinate system Q-$x_2y_2z_2$ with respect to the fixed coordinate system A-$x_0y_0z_0$ is

$$\boldsymbol{\varpi}_2=\left(\Omega-\frac{\Omega}{2}\theta_\eta^2-\frac{\Omega}{2}\theta_\xi^2+\theta_\eta\dot{\theta}_\xi\right)\mathbf{i}_2+\left(\dot{\theta}_\xi-\Omega\theta_\eta\right)\mathbf{j}_2+\left(\dot{\theta}_\eta+\Omega\theta_\xi\right)\mathbf{k}_2 \tag{22}$$

Therefore, the kinetic energies of the two plates can be derived as

$$\begin{aligned} T_{p1}&=\frac{1}{2}\int_{-h/2}^{h/2}\int_0^a\int_{-b/2}^{b/2}\rho_B\dot{\mathbf{r}}_{AM_2}{}^{\mathrm{T}}\dot{\mathbf{r}}_{AM_2}\mathrm{d}x_2\mathrm{d}y_2\mathrm{d}z_2 \\ &=\frac{1}{2}\int_{-h/2}^{h/2}\int_0^a\int_{-b/2}^{b/2}\rho_B\left[\mathrm{d}\mathbf{r}_{AM_2}/\mathrm{d}t+\boldsymbol{\varpi}_2\times\mathbf{r}_{AM_2}\right]^{\mathrm{T}}\left[\mathrm{d}\mathbf{r}_{AM_2}/\mathrm{d}t+\boldsymbol{\varpi}_2\times\mathbf{r}_{AM_2}\right]\mathrm{d}x_2\mathrm{d}y_2\mathrm{d}z_2 \\ &=\frac{1}{2}\int_{-h/2}^{h/2}\rho_B\begin{bmatrix} \frac{1}{3}a^3b\left(\dot{\theta}_{b\eta}{}^2-\Omega^2\theta_{b\eta}{}^2+2\Omega\theta_{b\xi}\dot{\theta}_{b\eta}+2\Omega\dot{\theta}_{b\xi}\theta_{b\eta}\right)+\frac{1}{2}\Omega^2a^2\left(b^2\theta_{b\eta}+2bv_0\right) \\ +\frac{1}{3}b^3a\left(\dot{\theta}_{b\eta}{}^2+\dot{\theta}_{b\xi}{}^2+\Omega^2\theta_{b\eta}{}^2+\Omega^2\theta_{b\xi}{}^2+2\Omega\theta_{b\xi}\dot{\theta}_{b\eta}-2\Omega\dot{\theta}_{b\xi}\theta_{b\eta}\right) \\ +ab^2\left(\dot{\theta}_{b\eta}\dot{v}_0-\dot{\theta}_{b\xi}\dot{w}_0+\Omega\theta_{b\eta}\dot{w}_0-\Omega\dot{\theta}_{b\eta}w_0+\Omega\theta_{b\xi}\dot{v}_0-\Omega\dot{\theta}_{b\xi}v_0-\Omega^2\theta_{b\xi}w_0\right) \\ +ab\left(\dot{v}_0{}^2+\dot{w}_0{}^2+\Omega^2v_0{}^2+\Omega^2w_0{}^2+2\Omega v_0\dot{w}_0-2\Omega\dot{v}_0w_0\right)+ab^2\Omega^2\theta_{b\eta}v_0 \end{bmatrix}\mathrm{d}z_2 \\ &\quad+\frac{1}{2}\int_{-h/2}^{h/2}\int_0^a\int_{-b/2}^{b/2}\rho_B\begin{bmatrix} \dot{w}_p{}^2+2\left(\dot{w}_0+\Omega v_0\right)\dot{w}_p+2\left(\Omega\theta_{b\eta}-\dot{\theta}_{b\xi}\right)x_2\dot{w}_p \\ -2\Omega\left(\dot{v}_0-\Omega w_0\right)w_p-2\Omega\left(\dot{\theta}_{b\eta}+\Omega\theta_{b\xi}\right)x_2w_p \\ +\Omega^2w_p{}^2 \end{bmatrix}\mathrm{d}x_2\mathrm{d}y_2\mathrm{d}z_2 \end{aligned} \tag{23}$$

$$
\begin{aligned}
T_{p2} &= \frac{1}{2}\int_{-h/2}^{h/2}\int_{-a-2r_b}^{0}\int_{-b/2}^{b/2}\rho_B \dot{\mathbf{r}}_{AM_3}{}^{\mathrm{T}}\dot{\mathbf{r}}_{AM_3}\mathrm{d}x_2\mathrm{d}y_2\mathrm{d}z_2 \\
&= \frac{1}{2}\int_{-h/2}^{h/2}\int_{-a-2r_b}^{0}\int_{-b/2}^{b/2}\rho_B\left[\mathrm{d}\mathbf{r}_{AM_3}/\mathrm{d}t+\boldsymbol{\varpi}_2\times\mathbf{r}_{AM_3}\right]^{\mathrm{T}}\left[\mathrm{d}\mathbf{r}_{AM_3}/\mathrm{d}t+\boldsymbol{\varpi}_2\times\mathbf{r}_{AM_3}\right]\mathrm{d}x_2\mathrm{d}y_2\mathrm{d}z_2 \\
&= \frac{1}{2}\int_{-h/2}^{h/2}\rho_B\begin{bmatrix}
\frac{1}{3}a^3b\left(\dot{\theta}_{b\eta}{}^2-\Omega^2\theta_{b\eta}{}^2+2\Omega\theta_{b\xi}\dot{\theta}_{b\eta}+2\Omega\dot{\theta}_{b\xi}\theta_{b\eta}\right)+\frac{1}{2}\Omega^2a^2\left(b^2\theta_{b\eta}+2bv_0\right) \\
+\frac{1}{3}b^3a\left(\dot{\theta}_{b\eta}{}^2+\dot{\theta}_{b\xi}{}^2+\Omega^2\theta_{b\eta}{}^2+\Omega^2\theta_{b\xi}{}^2+2\Omega\theta_{b\xi}\dot{\theta}_{b\eta}-2\Omega\dot{\theta}_{b\xi}\theta_{b\eta}\right) \\
+ab^2\left(\dot{\theta}_{b\eta}\dot{v}_0-\dot{\theta}_{b\xi}\dot{w}_0+\Omega\theta_{b\eta}\dot{w}_0-\Omega\dot{\theta}_{b\eta}w_0+\Omega\theta_{b\xi}\dot{v}_0-\Omega\dot{\theta}_{b\xi}v_0-\Omega^2\theta_{b\xi}w_0\right) \\
+ab\left(\dot{v}_0{}^2+\dot{w}_0{}^2+\Omega^2v_0{}^2+\Omega^2w_0{}^2+2\Omega v_0\dot{w}_0-2\Omega\dot{v}_0w_0\right)+ab^2\Omega^2\theta_{b\eta}v_0
\end{bmatrix}\mathrm{d}z_2 \\
&\quad+\frac{1}{2}\int_{-h/2}^{h/2}\int_{-a-2r_b}^{0}\int_{-b/2}^{b/2}\rho_B\begin{bmatrix}
\dot{w}_p{}^2+2\left(\dot{w}_0+\Omega v_0\right)\dot{w}_p+2\left(\Omega\theta_{b\eta}-\dot{\theta}_{b\xi}\right)x_2\dot{w}_p \\
-2\Omega\left(\dot{v}_0-\Omega w_0\right)w_p-2\Omega\left(\dot{\theta}_{b\eta}+\Omega\theta_{b\xi}\right)x_2w_p \\
+\Omega^2w_p{}^2
\end{bmatrix}\mathrm{d}x_2\mathrm{d}y_2\mathrm{d}z_2
\end{aligned}
\tag{24}
$$

According to the Kirchhoff plate theory, the deformation potential energies of the two plates are

$$
U_{p1}=\frac{1}{2}\int_{-h/2}^{h/2}\int_{0}^{a}\int_{-b/2}^{b/2}\begin{bmatrix}
\frac{z_2{}^2E_p}{1-\mu_p{}^2}\left(\frac{\partial^2w_p}{\partial x_2{}^2}\right)^2+\frac{2z_2{}^2E_p}{1+\mu_p}\left(\frac{\partial^2w_p}{\partial x_2\partial y_2}\right)^2 \\
+\frac{2z_2{}^2E_p\mu_p}{1-\mu_p{}^2}\left(\frac{\partial^2w_p}{\partial x_2{}^2}\right)\left(\frac{\partial^2w_p}{\partial y_2{}^2}\right)+\frac{z_2{}^2E_p}{1-\mu_p{}^2}\left(\frac{\partial^2w_p}{\partial y_2{}^2}\right)^2
\end{bmatrix}\mathrm{d}x_2\mathrm{d}y_2\mathrm{d}z_2 \tag{25}
$$

$$
U_{p2}=\frac{1}{2}\int_{-h/2}^{h/2}\int_{-a-2r_b}^{0}\int_{-b/2}^{b/2}\begin{bmatrix}
\frac{z_2{}^2E_p}{1-\mu_p{}^2}\left(\frac{\partial^2w_p}{\partial x_2{}^2}\right)^2+\frac{2z_2{}^2E_p}{1+\mu_p}\left(\frac{\partial^2w_p}{\partial x_2\partial y_2}\right)^2 \\
+\frac{2z_2{}^2E_p\mu_p}{1-\mu_p{}^2}\left(\frac{\partial^2w_p}{\partial x_2{}^2}\right)\left(\frac{\partial^2w_p}{\partial y_2{}^2}\right)+\frac{z_2{}^2E_p}{1-\mu_p{}^2}\left(\frac{\partial^2w_p}{\partial y_2{}^2}\right)^2
\end{bmatrix}\mathrm{d}x_2\mathrm{d}y_2\mathrm{d}z_2 \tag{26}
$$

Due to the rotation, the centrifugal potential energies of the two plates can be obtained as

$$
U_{p3}=\frac{1}{2}\int_{-h/2}^{h/2}\int_{0}^{a}\int_{-b/2}^{b/2}\left[\frac{\Omega^2}{2}\rho_p\left(a^2-y_2{}^2\right)\left(\frac{\partial^2w_p}{\partial y_2{}^2}\right)^2\right]\mathrm{d}x_2\mathrm{d}y_2\mathrm{d}z_2 \tag{27}
$$

$$
U_{p4}=\frac{1}{2}\int_{-h/2}^{h/2}\int_{-a-2r_b}^{0}\int_{-b/2}^{b/2}\left[\frac{\Omega^2}{2}\rho_p\left(a^2-y_2{}^2\right)\left(\frac{\partial^2w_p}{\partial y_2{}^2}\right)^2\right]\mathrm{d}x_2\mathrm{d}y_2\mathrm{d}z_2 \tag{28}
$$

Thus, the total kinetic energy and total potential energy of the two plates are

$$\begin{cases} T_p = T_{p1} + T_{p2} \\ U_p = U_{p1} + U_{p2} + U_{p3} + U_{p4} \end{cases} \tag{29}$$

In addition, the virtual work done by the elastic supporting forces is

$$\delta B_b = -\left[k\left(v_b \delta v_b + w_b \delta w_b \right) \right]\Big|_{x_1 = l_d} - \left[k\left(w_b \delta v_b - v_b \delta w_b \right) \right]\Big|_{x_1 = l_b - l_d} \tag{30}$$

where k is the elastic support stiffness.

2.4 *Governing equation*

As the vibration modes of double-bladed shaft structure are difficult to be given, the substructure modal synthesis method is adopted to divide the double-bladed shaft assembly into three substructures (a beam and two plates). Then, the motions of every substructure are approximated by a weighted superposition of admissible functions based on the assumed modes method. The boundary conditions of the beam are free at both ends, while those of the plates are clamped at one end and free at the other three ends.

The displacements of the beam are written as

$$\begin{cases} v_b\left(x_1, t \right) = \mathbf{\Phi}_b\left(x_1 \right) \left[\mathbf{Q}_{bv}\left(t \right) \right]^{\mathrm{T}} \\ w_b\left(x_1, t \right) = \mathbf{\Phi}_b\left(x_1 \right) \left[\mathbf{Q}_{bw}\left(t \right) \right]^{\mathrm{T}} \end{cases} \tag{31}$$

in which $\mathbf{Q}_{bv}(t)$ and $\mathbf{Q}_{bw}(t)$ are the generalized coordinate vectors of the beam; $\mathbf{\Phi}_b(x_1)$ is the mode function vector of the beam. Their specific expressions are

$$\begin{cases} \mathbf{Q}_{bv}\left(t \right) = \left\{ Qbv_1\left(t \right) \quad \cdots \quad Qbv_i\left(t \right) \quad \cdots \quad Qbv_m\left(t \right) \right\} \\ \mathbf{Q}_{bw}\left(t \right) = \left\{ Qbw_1\left(t \right) \quad \cdots \quad Qbw_i\left(t \right) \quad \cdots \quad Qbw_m\left(t \right) \right\} \end{cases} \tag{32}$$

$$\begin{cases} \mathbf{\Phi}_b\left(x_1 \right) = \left\{ \chi_1\left(x_1 \right) \quad \cdots \quad \chi_i\left(x_1 \right) \quad \cdots \quad \chi_m\left(x_1 \right) \right\} \\ \chi_1\left(x_1 \right) = 1, \chi_2\left(x_1 \right) = \sqrt{12}\left(\dfrac{x_1}{l_b} - \dfrac{1}{2} \right), \\ \chi_i\left(x_1 \right) = \cosh\left(\dfrac{\lambda_i x_1}{l_b} \right) + \cos\left(\dfrac{\lambda_i x_1}{l_b} \right) - \dfrac{\cosh\lambda_i - \cos\lambda_i}{\sinh\lambda_i - \sin\lambda_i} \left[\sinh\left(\dfrac{\lambda_i x_1}{l_b} \right) + \sin\left(\dfrac{\lambda_i x_1}{l_b} \right) \right] \quad i = 3, 4, \cdots m \end{cases} \tag{33}$$

where m is the total mode number of the beam; λ_i can be obtained form

$$\cos\lambda\cosh\lambda=1 \tag{34}$$

The displacements of the plates are expressed as

$$\begin{cases} w_{b1}\left(x_2,y_2,t\right)=\boldsymbol{\gamma}_b\left(x_2,y_2\right)\left[\mathbf{Q}_{bw1}\left(t\right)\right]^{\mathrm{T}} \\ w_{b2}\left(x_2,y_2,t\right)=\boldsymbol{\gamma}_b\left(x_2,y_2\right)\left[\mathbf{Q}_{bw2}\left(t\right)\right]^{\mathrm{T}} \end{cases} \tag{35}$$

where the generalized coordinate vector ($\mathbf{Q}_{bw1}$, $\mathbf{Q}_{bw2}$) and mode function vector $\boldsymbol{\gamma}_b$ are given by

$$\begin{cases} \mathbf{Q}_{bw1}\left(t\right)=\left\{QbwI_1\left(t\right) \quad \cdots \quad QbwI_j\left(t\right) \quad \cdots \quad QbwI_n\left(t\right)\right\} \\ \mathbf{Q}_{bw2}\left(t\right)=\left\{QbwII_1\left(t\right) \quad \cdots \quad QbwII_j\left(t\right) \quad \cdots \quad QbwII_n\left(t\right)\right\} \end{cases} \tag{36}$$

$$\boldsymbol{\gamma}_b\left(x_2,y_2\right)=\left\{\varsigma_1\left(x_2,y_2\right) \quad \cdots \quad \varsigma_j\left(x_2,y_2\right) \quad \cdots \quad \varsigma_n\left(x_2,y_2\right)\right\} \tag{37}$$

in which n is the total mode number of the plates; the mode function ς_j is

$$\varsigma_j\left(x_2,y_2\right)=\phi_j\left(x_2\right)\varphi_j\left(y_2\right) \tag{38}$$

where

$$\phi_j\left(x_2\right)=\cosh\left(\alpha_j x_2\right)-\cos\left(\alpha_j x_2\right)-c_j\left[\sinh\left(\alpha_j x_2\right)-\sin\left(\alpha_j x_2\right)\right] \tag{39}$$

$$\begin{cases} \varphi_1\left(y_2\right)=1,\varphi_2\left(y_2\right)=1-\dfrac{2y_2}{b} \\ \varphi_j\left(y_2\right)=\cosh(\beta_j y_2)+\cos\left(\beta_j y_2\right)-d_j\left[\sinh(\beta_j y_2)+\sin\left(\beta_j y_2\right)\right] \quad j=3,4,\cdots n \end{cases} \tag{40}$$

in which α_j, β_j, c_j and d_j satisfy

$$\begin{cases} \cosh\left(\alpha_j a\right)\cos\left(\alpha_j a\right)=-1 \\ c_j=\dfrac{\cos\left(\alpha_j a\right)+\cosh\left(\alpha_j a\right)}{\sin\left(\alpha_j a\right)+\sinh\left(\alpha_j a\right)}, \\ j=1,2,\cdots,n \end{cases} \quad \begin{cases} \cosh\left(\beta_j b\right)\cos\left(\beta_j b\right)=1 \\ d_j=\dfrac{\cos\left(\beta_j b\right)-\cosh\left(\beta_j b\right)}{\sin\left(\beta_j b\right)-\sinh\left(\beta_j b\right)} \\ j=3,4,\cdots,n \end{cases} \tag{41}$$

According to the Lagrange equation

$$\frac{\mathrm{d}}{\mathrm{d}t}\left(\frac{\partial L}{\partial\dot{q}_i}\right)-\frac{\partial L}{\partial q_i}=0 \tag{34}$$

the governing equation of double-bladed shaft assembly is

$$\mathbf{M}\ddot{\mathbf{q}}\left(t\right)+\mathbf{G}\dot{\mathbf{q}}\left(t\right)+\mathbf{K}\mathbf{q}\left(t\right)=\mathbf{0} \tag{35}$$

where

$$\mathbf{q}(t)=\left\{\mathbf{Q}_{bv}(t)\quad \mathbf{Q}_{bw}(t)\quad \mathbf{Q}_{bw1}(t)\quad \mathbf{Q}_{bw2}(t)\right\}^{\mathrm{T}} \tag{36}$$

$$\mathbf{M}=\begin{bmatrix}\mathbf{M}_{11} & \mathbf{0} & \mathbf{0} & \mathbf{0}\\ \mathbf{0} & \mathbf{M}_{22} & \mathbf{M}_{23} & \mathbf{M}_{24}\\ \mathbf{0} & \mathbf{M}_{32} & \mathbf{M}_{33} & \mathbf{0}\\ \mathbf{0} & \mathbf{M}_{42} & \mathbf{0} & \mathbf{M}_{44}\end{bmatrix} \tag{37}$$

$$\mathbf{G}=\begin{bmatrix}\mathbf{0} & \mathbf{G}_{12} & \mathbf{G}_{13} & \mathbf{G}_{14}\\ \mathbf{G}_{21} & \mathbf{0} & \mathbf{0} & \mathbf{0}\\ \mathbf{G}_{31} & \mathbf{0} & \mathbf{0} & \mathbf{0}\\ \mathbf{G}_{41} & \mathbf{0} & \mathbf{0} & \mathbf{0}\end{bmatrix} \tag{38}$$

$$\mathbf{K}=\begin{bmatrix}\mathbf{K}_{11} & \mathbf{K}_{12} & \mathbf{0} & \mathbf{0}\\ \mathbf{K}_{21} & \mathbf{K}_{22} & \mathbf{K}_{23} & \mathbf{K}_{24}\\ \mathbf{0} & \mathbf{K}_{32} & \mathbf{K}_{33} & \mathbf{0}\\ \mathbf{0} & \mathbf{K}_{42} & \mathbf{0} & \mathbf{K}_{44}\end{bmatrix} \tag{39}$$

in which the elements in stiffness matrix **K**, gyroscopic matrix **G** and mass matrix **M** are given in **Appendix**.

Setting

$$\mathbf{p}(t)=\bar{\mathbf{p}}e^{\mathrm{i}\omega t},\ \ \mathrm{i}=\sqrt{-1} \tag{40}$$

and substituting Eq. (40) into Eq. (35) yields

$$\left(\omega^2\mathbf{M}+\mathrm{i}\omega\mathbf{G}+\mathbf{K}\right)\bar{\mathbf{p}}e^{\mathrm{i}\omega t}=\mathbf{0} \tag{41}$$

For non-zero solution condition, one has

$$\left|\omega^2\mathbf{M}+\mathrm{i}\omega\mathbf{G}+\mathbf{K}\right|=0 \tag{42}$$

From this, the natural frequencies ω can be obtained by solving Eq. (42).

Moreover, the backward travelling wave frequency (ω_b) and forward travelling wave frequency (ω_f) of the double-bladed shaft assembly are given by

$$\begin{cases}\omega_b=\omega+\Omega\\ \omega_f=\left|\omega-\Omega\right|\end{cases} \tag{43}$$

3. Results and discussions

In this section, the convergence analysis, validation analysis, and parameter analysis are conducted in turn. Unless otherwise stated, the radius (r_b) and length (l_b) of the beam are 0.02m and 1m, respectively; the thickness (h), width (b) and length (a) of the plates are 0.02m, 0.4m and 0.5m, respectively; the connection point Q is located at $d = l_b/2$; the elastic supports are located at the ends (A, B) of the shaft, namely, $l_d = 0$; the elastic support stiffness (k) is 2×10^9 N/m. Moreover, the material parameters are E_{gpl} = 1.01TPa, E_m = 130GPa, μ_{gpl} = 0.186, μ_m= 0.34, ρ_{gpl} = 1062.5kg/m^3, ρ_m = 8960kg/m^3, $W_{gplb}^{\mathrm{T}} = W_{gplp}^{\mathrm{T}}$ = 1%, $l_b/t_b = l_p/t_p = 10^3$, $l_b/\kappa_b = l_p/\kappa_p$ = 2 and $e_b = e_p$ = 0.1. The porosity distribution patterns (III_b, III_p) and GPL distribution patterns (O_b, O_p) are taken as an example if not specified in the following analysis

3.1 *Convergence analysis*

Table 1 lists the variation of the first four natural frequencies with the mode numbers of the beam and plates. It can be found that the free vibration results tend to be convergent at m = 16, n = 6 which will be used in the following calculations.

Table 1 Natural frequencies ω (rad/s) of the double-bladed shaft assembly with different mode numbers.

Frequency	m = 16 n = 5	m = 15 n = 6	**m = 16** **n = 6**	m = 17 n = 6	m = 16 n = 7
ω_1	48.03	47.91	**48.02**	48.00	48.01
ω_2	74.37	73.49	**73.66**	73.63	73.27
ω_3	130.55	127.91	**130.55**	130.13	130.55
ω_4	335.85	335.38	**335.65**	335.63	335.39

3.2 *Validation analysis*

Because there are no available data in open literature for validation study, the commercial software ANSYS is adopted in this paper to conduct the modal analysis of the double-bladed shaft assembly on basis of finite element (FE) method. Solid185 element and combin14 element are adopted and the total numbers of element and node are 6232 and 8208, respectively. Moreover, the

porosity distribution patterns (II_b, II_p) and GPL distribution patterns (U_b, U_p) are considered in this part. From table 2, it is obvious that the theoretical and FE results have great agreement, which implies that the present modeling and free vibration analysis is accurate

Table 2 Comparison of natural frequencies ω (rad/s) between theoretical and FE results.

Frequency	$W_{gplb}^{T} = W_{gplp}^{T}$	Present	FE (rad/s)	Error
ω_1	0	41.13	39.25	4.58%
	0.33%	45.29	43.27	4.45%
	0.67%	49.20	46.97	4.53%
	1%	52.56	50.40	4.11%
ω_2	0	63.06	65.51	3.89%
	0.33%	69.46	72.18	3.91%
	0.67%	75.48	78.29	3.73%
	1%	80.66	83.95	4.08%
ω_3	0	107.76	111.49	3.46%
	0.33%	119.69	122.97	2.74%
	0.67%	133.06	133.50	0.33%
	1%	139.43	143.30	2.78%

3.3 *Parameter analysis*

For this part, both the graphic and tabular form are used to examine the effects of material parameters and structural parameters on the vibration behaviors of the double-bladed shaft assembly. To simplify the following presentation, LTR is for length-to-thickness ratio; LWR is for length-to-width ratio; LRR is for length-to-radius ratio; WTR is for width-to-thickness ratio; TWF is for travelling wave frequency; TWFs is for travelling wave frequencies.

3.3.1 *Material parametric analysis*

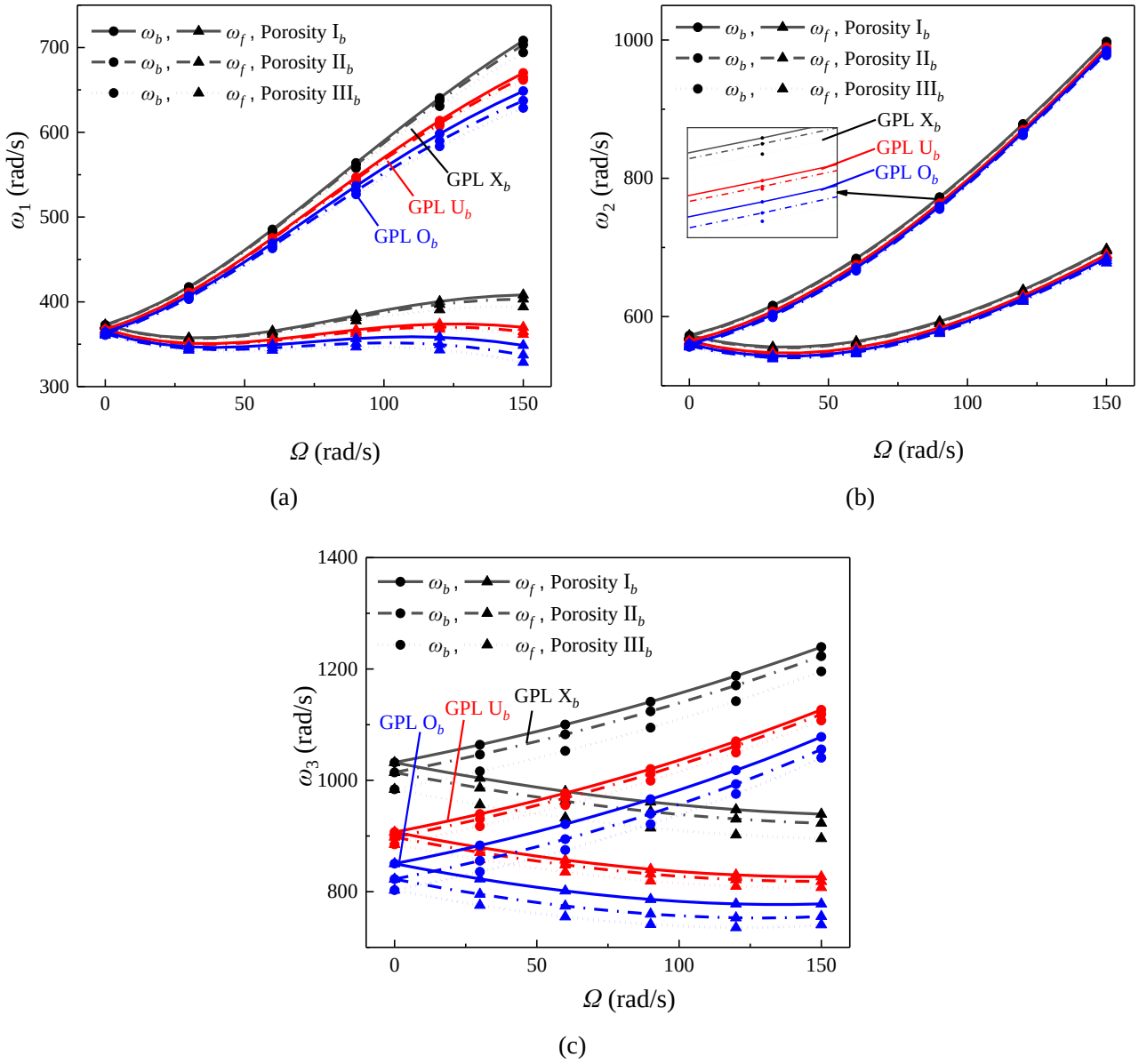

Fig. 4 Effects of GPL distribution and porosity distribution in the beam on the first three TWFs of the double-bladed shaft assembly.

Fig. 4 plots the variation of the first three TWFs of the double-bladed shaft assembly with rotating speed for different distributions of GPLs and porosity in the beam. In the figures, different line-types stand for different porosity distribution patterns; different line-colors stand for different GPL distribution patterns; circular mark and triangle mark in the lines stand for forward TWF and backward TWF, respectively. One can see that the first two forward TWFs decrease first and then rise with the rotating speed, while third forward TWFs have a monotonous reduction. Another observation is that the first three backward TWFs always increase with the rotating speed.

In addition, the GPL distribution pattern X_b provide greater TWFs than the other GPL distributions, while porosity distribution pattern I_b give the largest TWFs among the three porosity distributions. This implies that arranging smaller pores and more GPLs around the surfaces of the beam are effective to enhance the structural stiffness. Obviously, the GPL distributions in the beam have more significant influence than the porosity distributions on the free vibration results. Moreover, the GPL distribution and porosity distribution of the beam mainly affect the first TWF under high rotating speed ($\Omega > 100$ rad/s), and third TWF.

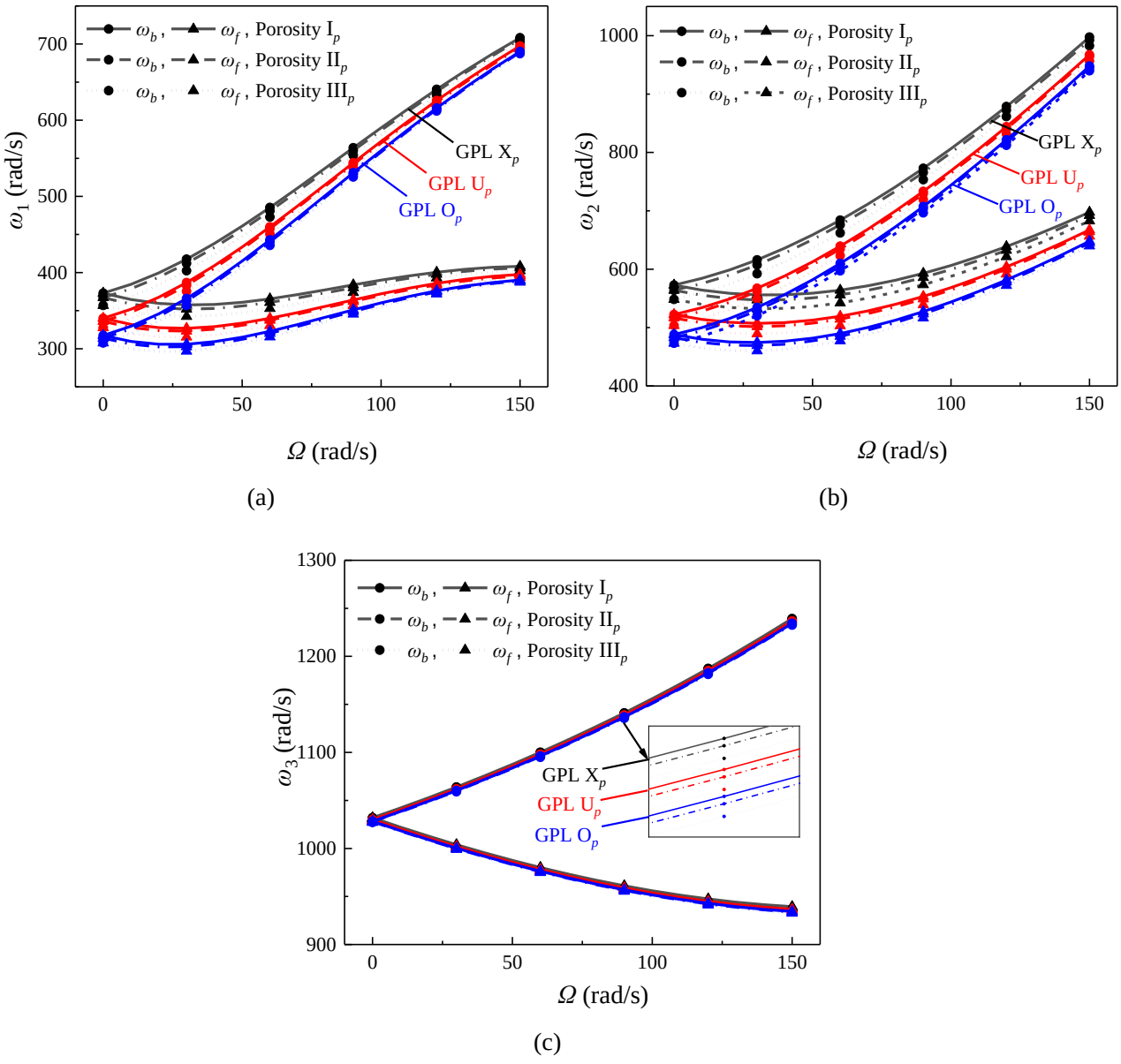

Fig. 5 Effects of GPL distribution and porosity distribution in the plates on the first three TWFs of the double-bladed shaft assembly.

Fig. 5 displays the variation of the first three TWFs of the double-bladed shaft assembly with rotating speed for different distributions of GPLs and porosity in the plates. Results show that the GPL distribution pattern X_p and porosity distribution pattern I_p have larger TWFs compared to the other GPL and porosity distributions, severally. This indicates that smaller pores and more GPLs around the surfaces of the plates can be applied to improve the mechanical performance of the double-bladed shaft assembly. Similarly, the GPL distributions in the plates give a greater impact than the porosity distributions on the free vibration results. The GPL distribution and porosity distribution of the plates primarily affect the first TWF under low rotating speed ($\Omega < 100$ rad/s), and second TWF.

As the material parameters have the same effects on the forward TWFs and backward TWFs, only the backward TWFs in three typical rotating case: 0rad/s (stationary), 50rad/s (low rotating speed) and 150rad/s (high rotating speed) are adopted in the following material parameter study (Table 3-6).

Table 3 lists the variation of the first three backward TWFs of the double-bladed shaft assembly with rotating speed for different GPL weight fractions, where ($p = 0$, $q = f$) represents that only the beam is reinforced; ($p = f$, $q = 0$) represents that only the plates are reinforced, and ($p = q = f$) represents that both the beam and plates are equally reinforced by GPLs. As can be seen, the increase of the GPL weight fraction leads to increased TWFs, which indicates that adding more GPLs into the matrix can give a hand to achieve better mechanical performance. In addition, the first TWFs at stationary and low rotating speed cases ($\Omega = 0$ and 50 rad/s), and the second TWF are mainly influenced by the GPL weight fraction in the plates. Oppositely, the first TWF at high rotating speed case ($\Omega = 150$ rad/s), and the third TWF are majorly affected by the GPL weight fraction in the beam.

Table 3 Effect of GPL weight fraction on the first three backward TWFs (rad/s) of the double-bladed shaft system with different rotating speeds (rad/s).

Frequency	Ω	$W_{gplp}^{T} = p$ $W_{gplb}^{T} = q$	f = 0%	f = 0.33%	f = 0.67%	f = 1%
ω_1	0	p = 0, q = f	253.01	254.38	255.08	256.45
		p = f, q = 0	253.01	268.53	283.05	296.34
		p = q = f	253.01	270.16	285.91	301.72
	50	p = 0, q = f	302.51	305.77	307.46	310.67
		p = f, q = 0	302.51	314.11	325.23	335.62
		p = q = f	302.51	317.67	331.07	345.95
	150	p = 0, q = f	403.46	421.58	431.98	450.91
		p = f, q = 0	403.46	409.79	416.02	421.99
		p = q = f	403.46	428.11	445.18	471.00
ω_2	0	p = 0, q = f	387.91	390.16	391.39	393.76
		p = f, q = 0	387.91	411.79	434.29	455.02
		p = q = f	387.91	414.30	438.57	462.82
	50	p = 0, q = f	439.20	441.76	443.22	445.98
		p = f, q = 0	439.20	459.89	479.70	498.19
		p = q = f	439.20	462.66	484.38	506.57
	150	p = 0, q = f	734.56	739.75	741.73	744.14
		p = f, q = 0	734.56	744.72	754.45	763.48
		p = q = f	734.56	751.01	764.69	779.06
ω_3	0	p = 0, q = f	687.00	725.95	750.28	795.74
		p = f, q = 0	687.00	694.17	701.21	707.94
		p = q = f	687.00	733.54	765.87	820.25
	50	p = 0, q = f	695.78	734.07	758.04	802.88
		p = f, q = 0	695.78	703.03	710.16	716.97
		p = q = f	695.78	741.72	773.72	827.47
	150	p = 0, q = f	781.73	811.64	831.80	871.01
		p = f, q = 0	781.73	790.47	799.37	808.17
		p = q = f	781.73	819.77	847.96	895.57

Table 4 shows that the variation of the first three TWFs of the double-bladed shaft assembly with rotating speed for different GPL LTRs. It can be seen that the TWFs increase significantly with the GPL LTR. For the same content of GPLs, the larger value of the GPL LTR stands for a thinner

GPL. Thus, it implies that better reinforced effect occurs when thinner GPLs are adopted. Moreover, it can be found that the effects of the GPL LTR in the plates are sensitive to the first TWFs at stationary and low rotating speed cases (Ω = 0 and 50 rad/s), and second TWF. Oppositely, the effects of the GPL LTR in the beam are impressible to the first TWF at high rotating speed case (Ω = 150 rad/s), and third TWF.

Table 4 Effect of GPL LTR on the first three backward TWFs (rad/s) of the double-bladed shaft system with different rotating speeds (rad/s).

Frequency	Ω	$L_p/t_p = p$ $L_b/t_b = q$	f = 10	f = 100	f = 500	f = 1000
First	0	p = 10, $q = f$	297.58	297.75	298.22	298.82
		$p = f$, q = 10	297.58	300.09	300.40	300.44
		$p = q = f$	297.58	300.26	301.06	301.72
	50	p = 10, $q = f$	341.31	341.65	342.53	343.72
		$p = f$, q = 10	341.31	343.23	343.47	344.50
		$p = q = f$	341.31	343.58	344.71	345.95
	150	p = 10, $q = f$	458.28	460.25	463.76	470.32
		$p = f$, q = 10	458.28	458.84	458.91	458.92
		$p = q = f$	458.28	460.82	464.41	471.00
Second	0	p = 10, $q = f$	456.49	456.78	457.39	458.40
		$p = f$, q = 10	456.49	460.34	460.81	460.87
		$p = q = f$	456.49	460.63	461.73	462.82
	50	p = 10, $q = f$	500.56	500.89	501.51	502.64
		$p = f$, q = 10	500.56	503.98	504.40	504.46
		$p = q = f$	500.56	504.32	505.37	506.57
	150	p = 10, $q = f$	774.75	775.20	775.54	776.75
		$p = f$, q = 10	774.75	776.72	776.97	777.00
		$p = q = f$	774.75	777.18	777.79	779.06
Third	0	p = 10, $q = f$	790.78	795.85	803.32	820.25
		$p = f$, q = 10	790.78	790.78	790.78	790.78
		$p = q = f$	790.78	795.85	803.32	820.25
	50	p = 10, $q = f$	798.38	803.38	810.73	827.44

		$p = f, q = 10$	798.38	798.41	798.42	798.42
		$p = q = f$	798.38	803.41	810.77	827.47
	150	$p = 10, q = f$	870.07	874.33	880.80	895.32
		$p = f, q = 10$	870.07	870.34	870.37	870.38
		$p = q = f$	870.07	874.58	881.07	895.57

The variation of the first three TWFs of the double-bladed shaft assembly with rotating speed for different GPL LWRs is present in Table 5, where the GPL length remains constant. As can be seen, a decrease of GPL LWR results in the significant rise of the TWFs. Actually, the smaller value of GPL LWR represents that individual GPL has a larger surface area, which can lead to a better load transfer capability. Besides, the first TWFs at stationary and low rotating speed cases (Ω = 0 and 50 rad/s), and second TWF are mainly influenced by the GPL LWR in the plates. Oppositely, the first TWF at high rotating speed case (Ω = 150 rad/s), and third TWF are chiefly impacted by the GPL LWR in the beam.

Table 5 Effect of GPL LWR on the first three backward TWFs (rad/s) of the double-bladed shaft system with different rotating speeds (rad/s).

Frequency	Ω	$L_p/\kappa_p = p$ $L_b/\kappa_b = q$	f = 1	f = 2	f = 4	f = 8
First	0	$p = 1, q = f$	302.42	302.35	302.22	301.96
		$p = f, q = 1$	302.42	301.78	301.23	300.95
		$p = q = f$	302.42	301.72	301.04	300.51
	50	$p = 1, q = f$	347.21	347.16	347.06	346.86
		$p = f, q = 1$	347.21	346.00	344.96	344.42
		$p = q = f$	347.21	345.95	344.81	344.08
	150	$p = 1, q = f$	477.08	471.02	466.01	463.27
		$p = f, q = 1$	477.08	477.06	477.03	476.97
		$p = q = f$	477.08	471.00	465.96	463.17
Second	0	$p = 1, q = f$	463.90	463.80	463.60	463.21
		$p = f, q = 1$	463.90	462.91	462.09	461.66
		$p = q = f$	463.90	462.82	461.80	460.98
	50	$p = 1, q = f$	507.73	507.65	507.47	507.12

		$p = f, q = 1$	507.73	506.66	505.77	505.30
		$p = q = f$	507.73	506.57	505.51	504.69
		$p = 1, q = f$	780.01	779.96	779.85	779.64
	150	$p = f, q = 1$	780.01	779.11	778.36	777.87
		$p = q = f$	780.01	779.06	778.20	777.51
		$p = 1, q = f$	835.51	820.25	808.08	801.33
	0	$p = f, q = 1$	835.51	835.51	835.51	835.51
		$p = q = f$	835.51	820.25	808.08	801.33
		$p = 1, q = f$	842.53	827.47	815.47	808.82
Third	50	$p = f, q = 1$	842.53	842.53	842.53	842.53
		$p = q = f$	842.53	827.47	815.47	808.81
		$p = 1, q = f$	908.85	895.57	885.07	879.31
	150	$p = f, q = 1$	908.85	908.85	908.84	908.82
		$p = q = f$	908.85	895.57	885.05	879.26

Table 6 illustrates the variation of the first three TWFs of the double-bladed shaft assembly with rotating speed for different porosity coefficients. It is obvious that the TWF has a noticeable reduction with the increase of the porosity coefficient, which is because the pores can weak the assembly. Similar, the porosity coefficient of the plates mainly impacts the first TWFs at stationary and low rotating speed cases (Ω = 0 and 50 rad/s), and second TWF. Oppositely, the porosity coefficient of the beam primarily effects the first TWF at high rotating speed case (Ω = 150 rad/s), and third TWF.

Moreover, there is an interesting phenomenon. The solitary rise of porosity coefficient in the plates may lead to the increase of the first TWF at high rotating speed case (Ω = 150 rad/s), and third TWF. It indicates that lighter assembly may have better mechanical performance in some cases.

Table 6 Effect of porosity coefficient on the first three backward TWFs (rad/s) of the double-bladed shaft system with different rotating speeds (rad/s).

Frequency	Ω	$e_p = p$ $e_b = q$	f = 0.1	f = 0.2	f = 0.3	f = 0.4

First	0	$p = 0.1, q = f$	301.72	299.37	296.19	293.87
		$p = f, q = 0.1$	301.72	290.98	279.22	266.40
		$p = q = f$	301.72	288.97	275.25	261.75
	50	$p = 0.1, q = f$	345.95	341.46	335.42	330.98
		$p = f, q = 0.1$	345.95	338.30	329.95	320.91
		$p = q = f$	345.95	334.27	321.52	310.36
	150	$p = 0.1, q = f$	471.00	449.00	422.35	403.80
		$p = f, q = 0.1$	471.00	473.65	476.44	479.43
		$p = q = f$	471.00	452.14	429.83	416.53
Second	0	$p = 0.1, q = f$	462.82	459.26	454.94	451.94
		$p = f, q = 0.1$	462.82	446.53	428.87	409.72
		$p = q = f$	462.82	443.27	422.24	401.52
	50	$p = 0.1, q = f$	506.57	502.72	498.18	495.06
		$p = f, q = 0.1$	506.57	492.34	477.10	460.82
		$p = q = f$	506.57	488.70	469.60	451.24
	150	$p = 0.1, q = f$	779.06	774.89	764.96	749.03
		$p = f, q = 0.1$	779.06	770.89	762.21	753.11
		$p = q = f$	779.06	767.51	754.72	743.21
Third	0	$p = 0.1, q = f$	820.25	768.30	711.74	675.51
		$p = f, q = 0.1$	820.25	832.99	847.03	862.67
		$p = q = f$	820.25	780.35	735.42	711.57
	50	$p = 0.1, q = f$	827.47	776.29	720.76	685.33
		$p = f, q = 0.1$	827.47	839.92	853.67	869.02
		$p = q = f$	827.47	788.00	743.63	720.01
	150	$p = 0.1, q = f$	895.57	851.80	810.27	793.56
		$p = f, q = 0.1$	895.57	905.77	917.31	930.45
		$p = q = f$	895.57	860.46	822.08	801.54

From the above, it can be told that the material parameters (GPL weight fraction, GPL LTR, GPL LWR, GPL distribution pattern, porosity distribution pattern, porosity coefficient) in the plates play an important part in the first TWF in the case of low rotating speed, and second TWF. Oppositely, the material parameters in the beam take a significant role in the first TWF in the case

of high rotating speed, and third TWF.

3.3.2 *Structural parameter analysis*

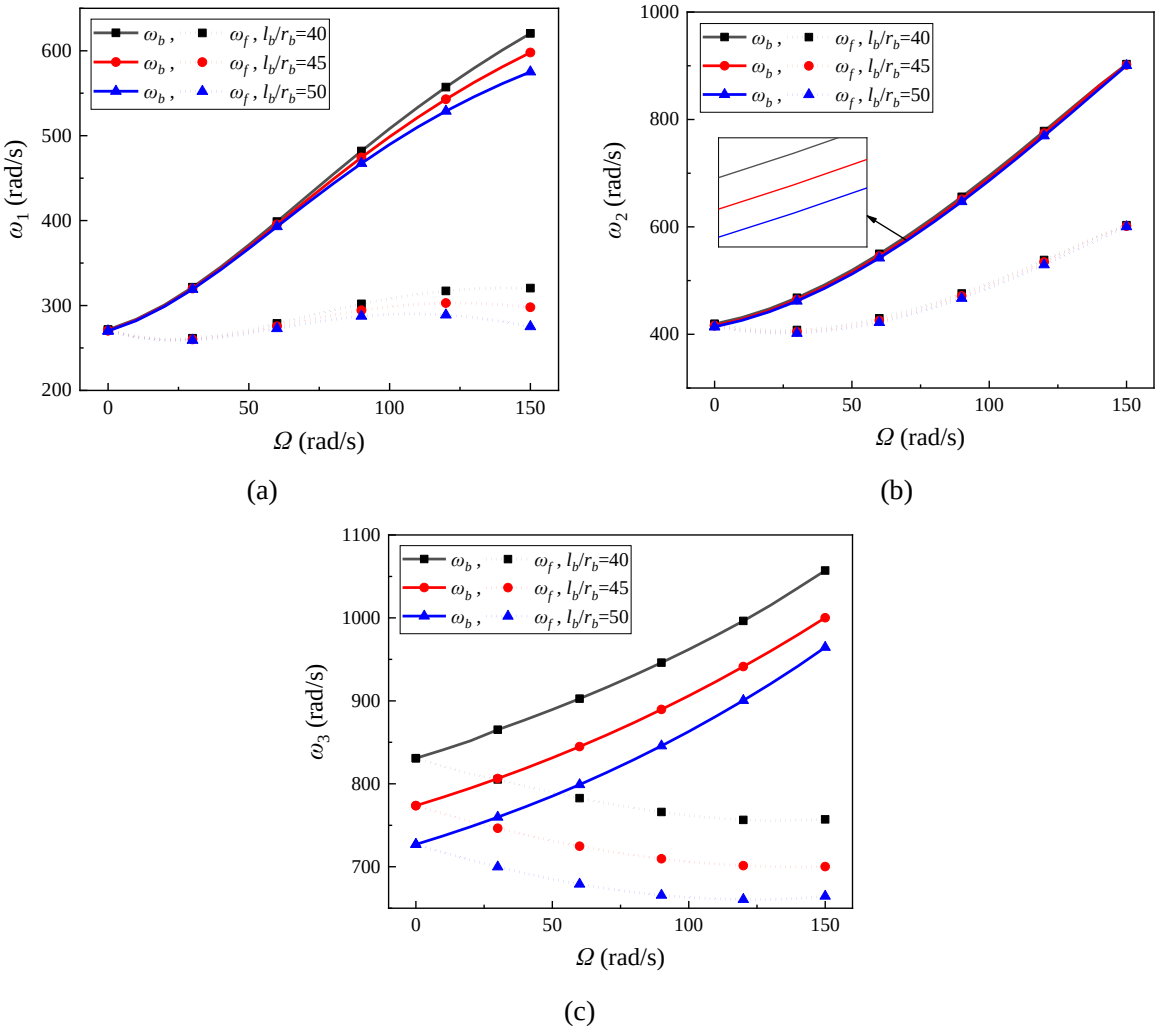

Fig. 6 Effect of beam LRR on the first three TWFs of the double-bladed shaft system.

Fig. 6 plots the variation of the first three TWFs of the double-bladed shaft assembly with rotating speed for different beam LRRs, where the beam radius remains constant. One can see that the TWFs decrease dramatically with the increase of beam LRR. This implies that shorter beam should be designed to enhance the structural stiffness of the double-bladed shaft assembly. Another observation is that the beam LRR mainly affects the first TWF in the case of high rotating speed, and third TWF.

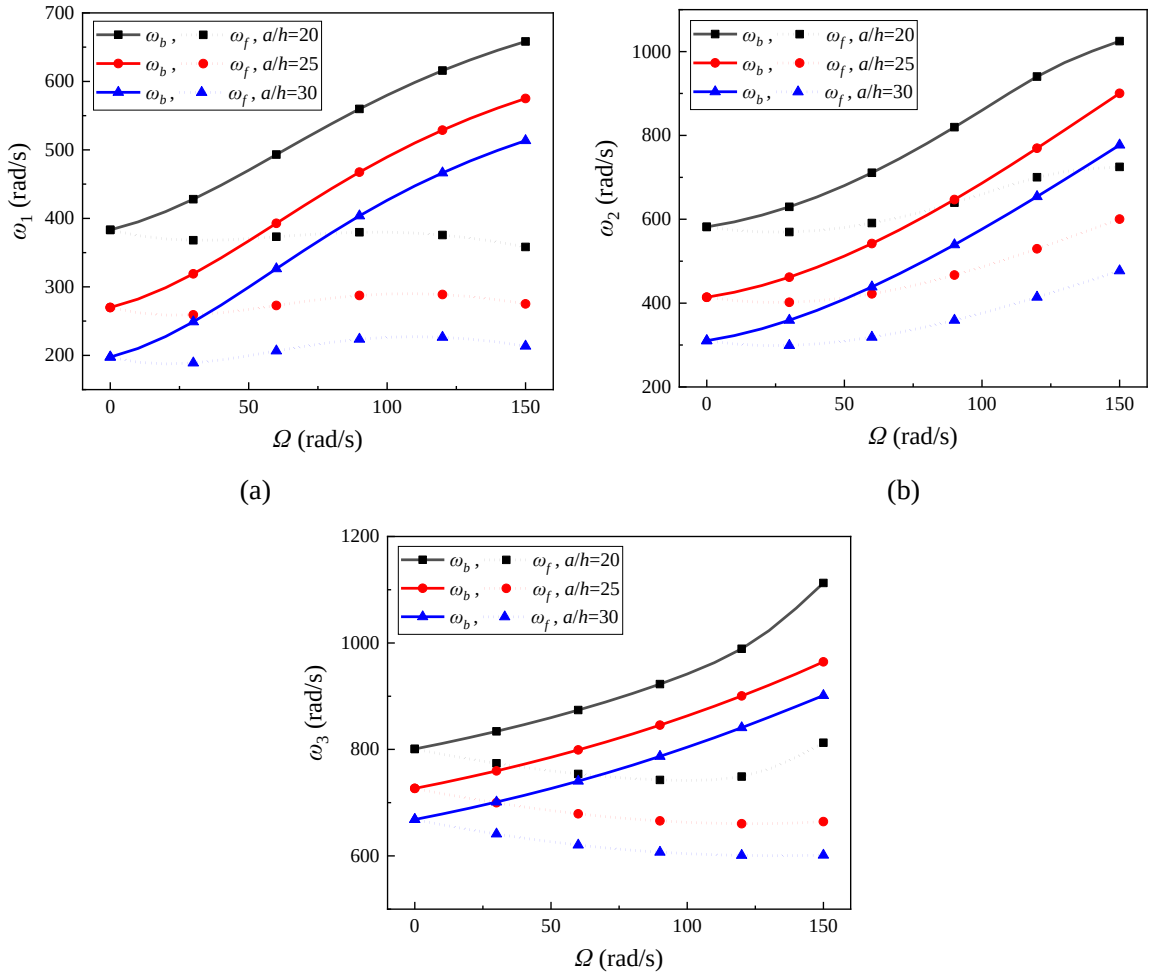

Fig. 7 Effect of plate LTR on the first three TWFs of the double-bladed shaft system.

Fig. 7 gives the variation of the first three TWFs of the double-bladed shaft assembly with rotating speed for different plate LTRs, where the plate thickness keeps constant. It is obviously that the TWFs rise dramatically with the decrease of plate LTR. This demonstrates that the plates should not be long size to achieve better mechanical performance.

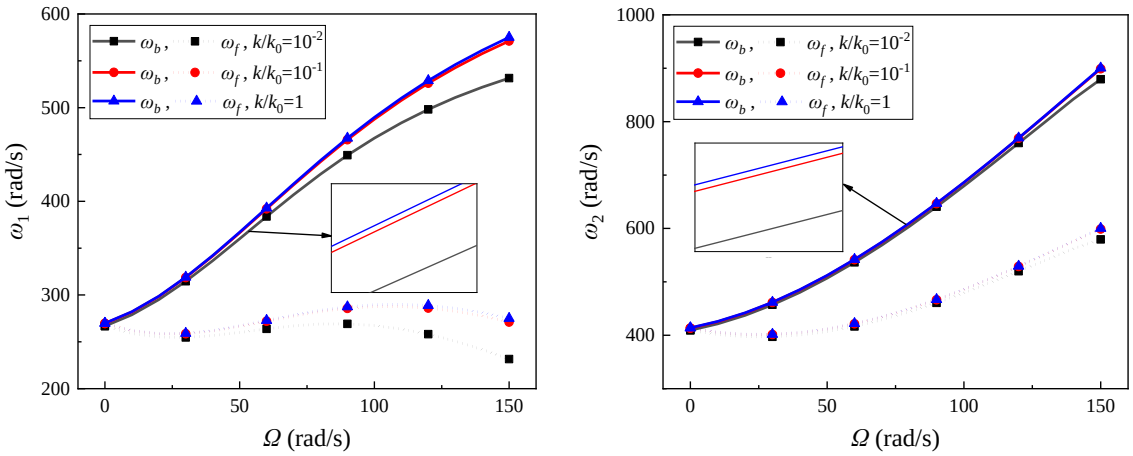

(a) (b)

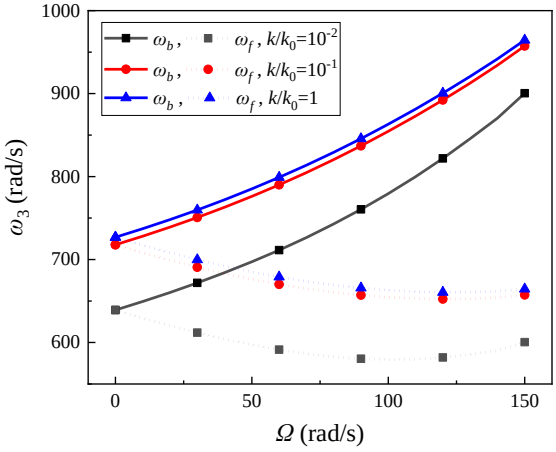

(c)

Fig. 8 Effect of support stiffness on the first three TWFs of the double-bladed shaft system.

Fig. 8 shows the variation of the first three TWFs of the double-bladed shaft assembly with rotating speed for different support stiffnesses, where $k_0 = 2\times10^9$ N/m. It is seen that larger support stiffness can lead to increased TWFs. Moreover, the first TWF in the case of low rotating speed, and second TWF are impacted relatively little by the support stiffness.

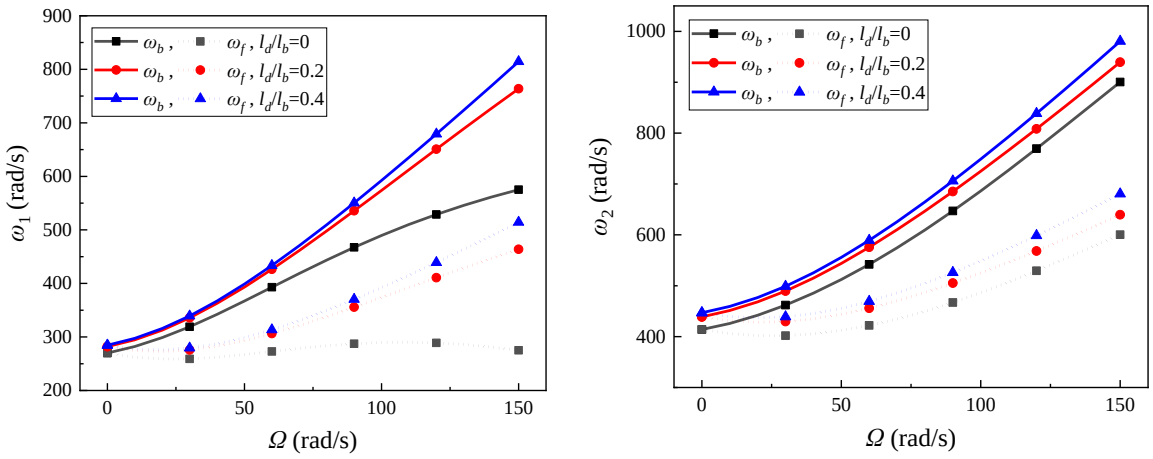

(a) (b)

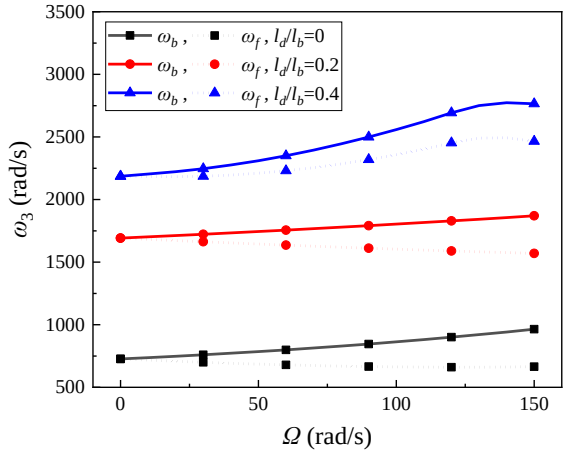

(c)

Fig. 8 Effect of support location on the first three TWFs of the double-bladed shaft system.

Fig. 8 illustrates the variation of the first three TWFs of the double-bladed shaft assembly with rotating speed for different support locations, where l_b keeps constant. We can see that the TWF increase with the distance between the support and the beam end. This means that the supports should be arranged near the plates to achieve better mechanical performance. In addition, the support location principally affects the first TWF in the case of high rotating speed, and third TWF.

4. Conclusions

This paper conducts the coupled modeling and free vibration analysis of a rotating porous double-bladed shaft assembly reinforced by GPLs. Based on the Euler-Bernoulli beam theory and the Kirchhoff plate theory, the coupled governing equation are derived by adopting the Lagrange equation. Then the substructure modal synthesis method and assumed modes method are utilized to obtain the free vibration results. Some conclusions worth mentioning are draw as follows:

(1) arranging smaller pores and more GPLs around the surfaces of the beam the plates are effective to enhance the structural stiffness;

(2) adding more GPLs into the matrix can give a hand to achieve better mechanical performance;

(3) better reinforced effect occurs when thinner GPLs with larger surface area are adopted;

(4) TWF has a noticeable reduction with the increase of the porosity coefficient;

(5) the material parameters in the plates play an important part in the first TWF in the case of low rotating speed, and second frequency, while those in the beam take a significant role in the first TWF in the case of high rotating speed, and third frequency;

(6) the beam and plates with shorter lengths can be designed to enhance structural performance;

(7) the supports with larger stiffness should be arranged near the plates to achieve better mechanical performance.

Funding

This project is supported by the National Natural Science Foundation of China (No. 51805076, No. U1708255 and No. 51775093), National Science and Technology Major Project of China (J2019-I-0008-0008), and the Fundamental Research Funds for the Central Universities of China (N2105013).

Appendix

$$\mathbf{M}_{11}=2\pi\int_0^{r_b}\rho_b r\mathrm{d}r\int_0^{l_b}\boldsymbol{\Phi}_b{}^{\mathrm{T}}\boldsymbol{\Phi}_b\mathrm{d}x_1+\pi\int_0^{r_b}\rho_b r^3\mathrm{d}r\int_0^{l_b}\boldsymbol{\Phi}_b'^{\mathrm{T}}\boldsymbol{\Phi}_b'\mathrm{d}x_1 + \left[\frac{a^3b+b^3a}{3}\boldsymbol{\Phi}_b'^{\mathrm{T}}\boldsymbol{\Phi}_b'+ab^2\frac{\boldsymbol{\Phi}_b{}^{\mathrm{T}}\boldsymbol{\Phi}_b'+\boldsymbol{\Phi}_b'^{\mathrm{T}}\boldsymbol{\Phi}_b}{2}+ab\boldsymbol{\Phi}_b{}^{\mathrm{T}}\boldsymbol{\Phi}_b\right]\Bigg|_{x_1=d}\int_{-h/2}^{h/2}\rho_p\mathrm{d}z_2\,,$$

$$\mathbf{M}_{22}=2\pi\int_0^{r_b}\rho_b r\mathrm{d}r\int_0^{l_b}\boldsymbol{\Phi}_b{}^{\mathrm{T}}\boldsymbol{\Phi}_b\mathrm{d}x_1+\pi\int_0^{r_b}\rho_b r^3\mathrm{d}r\int_0^{l_b}\boldsymbol{\Phi}_b'^{\mathrm{T}}\boldsymbol{\Phi}_b'\mathrm{d}x_1 + \left[\frac{b^3a}{3}\boldsymbol{\Phi}_b'^{\mathrm{T}}\boldsymbol{\Phi}_b'+ab^2\frac{\boldsymbol{\Phi}_b{}^{\mathrm{T}}\boldsymbol{\Phi}_b'+\boldsymbol{\Phi}_b'^{\mathrm{T}}\boldsymbol{\Phi}_b}{2}+ab\boldsymbol{\Phi}_b{}^{\mathrm{T}}\boldsymbol{\Phi}_b\right]\Bigg|_{x_1=d}\int_{-h/2}^{h/2}\rho_p\mathrm{d}z_2\,,$$

$$\mathbf{M}_{23}=\int_{-h/2}^{h/2}\rho_p\mathrm{d}z_2\int_0^a\int_{-b/2}^{b/2}\boldsymbol{\Phi}_b{}^{\mathrm{T}}\Big|_{x_1=d}\boldsymbol{\Psi}_p\mathrm{d}x_2\mathrm{d}y_2+\int_{-h/2}^{h/2}\rho_p\mathrm{d}z_2\int_0^a\int_{-b/2}^{b/2}\boldsymbol{\Phi}_b'^{\mathrm{T}}\Big|_{x_1=d}x_2\boldsymbol{\Psi}_p\mathrm{d}x_2\mathrm{d}y_2\,,$$

$$\mathbf{M}_{32}=\int_{-h/2}^{h/2}\rho_p\mathrm{d}z_2\int_0^a\int_{-b/2}^{b/2}\boldsymbol{\Psi}_p{}^{\mathrm{T}}\boldsymbol{\Phi}_b\Big|_{x_1=d}\mathrm{d}x_2\mathrm{d}y_2+\int_{-h/2}^{h/2}\rho_p\mathrm{d}z_2\int_0^a\int_{-b/2}^{b/2}x_2\boldsymbol{\Psi}_p{}^{\mathrm{T}}\boldsymbol{\Phi}_b'\Big|_{x_1=d}\mathrm{d}x_2\mathrm{d}y_2\,,$$

$$\mathbf{M}_{33}=\int_{-h/2}^{h/2}\rho_p\mathrm{d}z_2\int_0^a\int_{-b/2}^{b/2}\boldsymbol{\Psi}_p{}^{\mathrm{T}}\boldsymbol{\Psi}_p\mathrm{d}x_2\mathrm{d}y_2\,,$$

$$\mathbf{M}_{24}=\int_{-h/2}^{h/2}\rho_B\mathrm{d}z_2\int_{-a-2r_b}^{0}\int_{-b/2}^{b/2}\boldsymbol{\Phi}_b{}^{\mathrm{T}}\Big|_{x_1=d}\boldsymbol{\Psi}_p\mathrm{d}x_2\mathrm{d}y_2+\int_{-h/2}^{h/2}\rho_p\mathrm{d}z_2\int_{-a-2r_b}^{0}\int_{-b/2}^{b/2}\boldsymbol{\Phi}_b'^{\mathrm{T}}\Big|_{x_1=d}x_2\boldsymbol{\Psi}_p\mathrm{d}x_2\mathrm{d}y_2\,,$$

$$\mathbf{M}_{42}=\int_{-h/2}^{h/2}\rho_p \mathrm{d}z_2\int_{-a-2r_b}^{0}\int_{-b/2}^{b/2}\boldsymbol{\Psi}_p{}^{\mathrm{T}}\boldsymbol{\Phi}_b\big|_{x_1=d}\,\mathrm{d}x_2\mathrm{d}y_2+\int_{-h/2}^{h/2}\rho_p \mathrm{d}z_2\int_{-a-2r_b}^{0}\int_{-b/2}^{b/2}x_2\boldsymbol{\Psi}_p{}^{\mathrm{T}}\boldsymbol{\Phi}_b'\big|_{x_1=d}\,\mathrm{d}x_2\mathrm{d}y_2\,,$$

$$\mathbf{M}_{44}=\int_{-h/2}^{h/2}\rho_p \mathrm{d}z_2\int_{-a-2r_b}^{0}\int_{-b/2}^{b/2}\boldsymbol{\Psi}_p{}^{\mathrm{T}}\boldsymbol{\Psi}_p\mathrm{d}x_2\mathrm{d}y_2\,,$$

$$\mathbf{C}_{12}=-4\pi\Omega\int_0^{r_S}\rho_b r\mathrm{d}r\int_0^{l_S}\boldsymbol{\Phi}_b{}^{\mathrm{T}}\boldsymbol{\Phi}_b\mathrm{d}x_1-\Omega\int_{-h/2}^{h/2}\rho_p\mathrm{d}z_2\left(\begin{array}{l}\dfrac{2b^3a}{3}\boldsymbol{\Phi}_b'^{\mathrm{T}}\boldsymbol{\Phi}_b'+ab^2\boldsymbol{\Phi}_b'^{\mathrm{T}}\boldsymbol{\Phi}_b\\ +ab^2\boldsymbol{\Phi}_b{}^{\mathrm{T}}\boldsymbol{\Phi}_b'+2ab\boldsymbol{\Phi}_b{}^{\mathrm{T}}\boldsymbol{\Phi}_b\end{array}\right)\Bigg|_{x_1=d},$$

$$\mathbf{C}_{13}=-2\Omega\int_{-h/2}^{h/2}\rho_p\mathrm{d}z_2\int_0^a\int_{-b/2}^{b/2}\boldsymbol{\Phi}_b{}^{\mathrm{T}}\big|_{x_1=d}\,\boldsymbol{\Psi}_p\mathrm{d}x_2\mathrm{d}y_2-2\Omega\int_{-h/2}^{h/2}\rho_p\mathrm{d}z_2\int_0^a\int_{-b/2}^{b/2}\boldsymbol{\Phi}_b'^{\mathrm{T}}\big|_{x_1=d}\,x_2\boldsymbol{\Psi}_p\mathrm{d}x_2\mathrm{d}y_2\,,$$

$$\mathbf{C}_{14}=-2\Omega\int_{-h/2}^{h/2}\rho_p\mathrm{d}z_2\int_{-a-2r_b}^{0}\int_{-b/2}^{b/2}\boldsymbol{\Phi}_b{}^{\mathrm{T}}\big|_{x_1=d}\,\boldsymbol{\Psi}_p\mathrm{d}x_2\mathrm{d}y_2-2\Omega\int_{-h/2}^{h/2}\rho_p\mathrm{d}z_2\int_{-a-2r_b}^{0}\int_{-b/2}^{b/2}\boldsymbol{\Phi}_b'^{\mathrm{T}}\big|_{x_1=d}\,x_2\boldsymbol{\Psi}_p\mathrm{d}x_2\mathrm{d}y_2\,,$$

$$\mathbf{C}_{21}=4\pi\Omega\int_0^{r_b}\rho_b r\mathrm{d}r\int_0^{l_b}\boldsymbol{\Phi}_b{}^{\mathrm{T}}\boldsymbol{\Phi}_b\mathrm{d}x_1+\Omega\int_{-h/2}^{h/2}\rho_p\mathrm{d}z_2\left(\begin{array}{l}\dfrac{2b^3a}{3}\boldsymbol{\Phi}_b'^{\mathrm{T}}\boldsymbol{\Phi}_b'+ab^2\boldsymbol{\Phi}_b'^{\mathrm{T}}\boldsymbol{\Phi}_b\\ +ab^2\boldsymbol{\Phi}_b{}^{\mathrm{T}}\boldsymbol{\Phi}_b'+2ab\boldsymbol{\Phi}_b{}^{\mathrm{T}}\boldsymbol{\Phi}_b\end{array}\right)\Bigg|_{x_1=d},$$

$$\mathbf{C}_{31}=2\Omega\int_{-h/2}^{h/2}\rho_p\mathrm{d}z_2\int_0^a\int_{-b/2}^{b/2}\boldsymbol{\Psi}_p{}^{\mathrm{T}}\boldsymbol{\Phi}_b\big|_{x_1=d}\,\mathrm{d}x_2\mathrm{d}y_2+2\Omega\int_{-h/2}^{h/2}\rho_p\mathrm{d}z_2\int_0^a\int_{-b/2}^{b/2}x_2\boldsymbol{\Psi}_p{}^{\mathrm{T}}\boldsymbol{\Phi}_b'\big|_{x_1=d}\,\mathrm{d}x_2\mathrm{d}y_2\,,$$

$$\mathbf{C}_{41}=2\Omega\int_{-h/2}^{h/2}\rho_B\mathrm{d}z_2\int_{-a-2r_b}^{0}\int_{-b/2}^{b/2}\boldsymbol{\Psi}_p{}^{\mathrm{T}}\boldsymbol{\Phi}_b\big|_{x_1=d}\,\mathrm{d}x_2\mathrm{d}y_2+2\Omega\int_{-h/2}^{h/2}\rho_p\mathrm{d}z_2\int_{-a-2r_b}^{0}\int_{-b/2}^{b/2}x_2\boldsymbol{\Psi}_p{}^{\mathrm{T}}\boldsymbol{\Phi}_b'\big|_{x_1=d}\,\mathrm{d}x_2\mathrm{d}y_2\,,$$

$$\begin{aligned}\mathbf{K}_{11}=&-2\Omega^2\pi\int_0^{r_S}\rho_b r\mathrm{d}r\int_0^{l_b}\boldsymbol{\Phi}_b{}^{\mathrm{T}}\boldsymbol{\Phi}_b\mathrm{d}x_1+\Omega^2\pi\int_0^{r_S}\rho_b r^3\mathrm{d}r\int_0^{l_b}\boldsymbol{\Phi}_b'^{\mathrm{T}}\boldsymbol{\Phi}_b'\mathrm{d}x_1\\&+\Omega^2\int_{-h/2}^{h/2}\rho_p\mathrm{d}z_2\left[\frac{a^3b-b^3a}{3}\boldsymbol{\Phi}_b'^{\mathrm{T}}\boldsymbol{\Phi}_b'-ab^2\frac{\boldsymbol{\Phi}_b{}^{\mathrm{T}}\boldsymbol{\Phi}_b'+\boldsymbol{\Phi}_b'^{\mathrm{T}}\boldsymbol{\Phi}_b}{2}-ab\boldsymbol{\Phi}_b{}^{\mathrm{T}}\boldsymbol{\Phi}_b\right]\Bigg|_{x_1=d},\\&+\pi\int_0^{r_b}\left(\frac{E_b r^3}{1-\mu_b{}^2}\right)\mathrm{d}r\int_0^{l_b}\boldsymbol{\Phi}_b''^{\mathrm{T}}\boldsymbol{\Phi}_b''\mathrm{d}x_1+\left(k_1\boldsymbol{\Phi}_b{}^{\mathrm{T}}\boldsymbol{\Phi}_b\right)\Big|_{x_1=l_d}+\left(k_2\boldsymbol{\Phi}_b{}^{\mathrm{T}}\boldsymbol{\Phi}_b\right)\Big|_{x_1=l_b-l_d}\end{aligned}$$

$$\mathbf{K}_{12}=\left(k_1\boldsymbol{\Phi}_b{}^{\mathrm{T}}\boldsymbol{\Phi}_b\right)\Big|_{x_1=l_d}+\left(k_2\boldsymbol{\Phi}_b{}^{\mathrm{T}}\boldsymbol{\Phi}_b\right)\Big|_{x_1=l_b-l_d},\quad \mathbf{K}_{21}=-\left(k_1\boldsymbol{\Phi}_b{}^{\mathrm{T}}\boldsymbol{\Phi}_b\right)\Big|_{x_1=l_d}-\left(k_2\boldsymbol{\Phi}_b{}^{\mathrm{T}}\boldsymbol{\Phi}_b\right)\Big|_{x_1=l_b-l_d},$$

$$\begin{aligned}\mathbf{K}_{22}=&-2\Omega^2\pi\int_0^{r_S}\rho_b r\mathrm{d}r\int_0^{l_S}\boldsymbol{\Phi}_b{}^{\mathrm{T}}\boldsymbol{\Phi}_b\mathrm{d}x_1+\Omega^2\pi\int_0^{r_S}\rho_b r^3\mathrm{d}r\int_0^{l_S}\boldsymbol{\Phi}_b'^{\mathrm{T}}\boldsymbol{\Phi}_b'\mathrm{d}x_1\\&-\Omega^2\int_{-h/2}^{h/2}\rho_p\mathrm{d}z_2\left[\frac{b^3a}{3}\boldsymbol{\Phi}_b'^{\mathrm{T}}\boldsymbol{\Phi}_b'+ab^2\frac{\boldsymbol{\Phi}_b{}^{\mathrm{T}}\boldsymbol{\Phi}_b'+\boldsymbol{\Phi}_b'^{\mathrm{T}}\boldsymbol{\Phi}_b}{2}+ab\boldsymbol{\Phi}_b{}^{\mathrm{T}}\boldsymbol{\Phi}_b\right]\Bigg|_{x_1=d},\\&+\pi\int_0^{r_b}\left(\frac{E_b r^3}{1-\mu_b{}^2}\right)\mathrm{d}r\int_0^{l_b}\boldsymbol{\Phi}_b''^{\mathrm{T}}\boldsymbol{\Phi}_b''\mathrm{d}x_1+\left(k_1\boldsymbol{\Phi}_b{}^{\mathrm{T}}\boldsymbol{\Phi}_b\right)\Big|_{x_1=l_d}+\left(k_2\boldsymbol{\Phi}_b{}^{\mathrm{T}}\boldsymbol{\Phi}_b\right)\Big|_{x_1=l_b-l_d}\end{aligned}$$

$$\mathbf{K}_{23}=-\Omega^2\int_{-h/2}^{h/2}\rho_p\mathrm{d}z_2\int_0^a\int_{-b/2}^{b/2}\boldsymbol{\Phi}_b^{\mathrm{T}}\big|_{x_1=d}\boldsymbol{\Psi}_p\mathrm{d}x_2\mathrm{d}y_2-\Omega^2\int_{-h/2}^{h/2}\rho_p\mathrm{d}z_2\int_0^a\int_{-b/2}^{b/2}\boldsymbol{\Phi}_b'^{\mathrm{T}}\big|_{x_1=d}x_2\boldsymbol{\Psi}_p\mathrm{d}x_2\mathrm{d}y_2,$$

$$\mathbf{K}_{32}=-\Omega^2\int_{-h/2}^{h/2}\rho_p\mathrm{d}z_2\int_0^a\int_{-b/2}^{b/2}\boldsymbol{\Psi}_p^{\mathrm{T}}\boldsymbol{\Phi}_b\big|_{x_1=d}\mathrm{d}x_2\mathrm{d}y_2-\Omega^2\int_{-h/2}^{h/2}\rho_p\mathrm{d}z_2\int_0^a\int_{-b/2}^{b/2}x_2\boldsymbol{\Psi}_p^{\mathrm{T}}\boldsymbol{\Phi}_b'\big|_{x_1=d}\mathrm{d}x_2\mathrm{d}y_2,$$

$$\begin{aligned}\mathbf{K}_{33}=&\int_{-h/2}^{h/2}\frac{z_2^2E_p}{1-\mu_p^2}\mathrm{d}z_2\int_0^a\int_{-b/2}^{b/2}\boldsymbol{\Psi}_{pxx}''^{\mathrm{T}}\boldsymbol{\Psi}_{pxx}''\mathrm{d}x_2\mathrm{d}y_2+\int_{-h/2}^{h/2}\frac{z_2^2E_p}{1-\mu_p^2}\mathrm{d}z_2\int_0^a\int_{-b/2}^{b/2}\boldsymbol{\Psi}_{pyy}''^{\mathrm{T}}\boldsymbol{\Psi}_{pyy}''\mathrm{d}x_2\mathrm{d}y_2\\&+\int_{-h/2}^{h/2}\frac{z_2^2E_p\mu_p}{1-\mu_p^2}\mathrm{d}z_2\int_0^a\int_{-b/2}^{b/2}\boldsymbol{\Psi}_{pyy}''^{\mathrm{T}}\boldsymbol{\Psi}_{pxx}''\mathrm{d}x_2\mathrm{d}y_2+\int_{-h/2}^{h/2}\frac{z_2^2E_p\mu_p}{1-\mu_p^2}\mathrm{d}z_2\int_0^a\int_{-b/2}^{b/2}\boldsymbol{\Psi}_{pxx}''^{\mathrm{T}}\boldsymbol{\Psi}_{pyy}''\mathrm{d}x_2\mathrm{d}y_2\\&+2\int_{-h/2}^{h/2}\frac{z_2^2E_p}{1+\mu_p}\mathrm{d}z_2\int_0^a\int_{-b/2}^{b/2}\boldsymbol{\Psi}_{pxy}''^{\mathrm{T}}\boldsymbol{\Psi}_{pxy}''\mathrm{d}x_2\mathrm{d}y_2+\frac{\Omega^2}{2}\int_{-h/2}^{h/2}\rho_p\mathrm{d}z_2\int_0^a\int_{-b/2}^{b/2}\left[\left(a^2-y_2^2\right)\boldsymbol{\Psi}_{pyy}''^{\mathrm{T}}\boldsymbol{\Psi}_{pyy}''\right]\mathrm{d}x_2\mathrm{d}y_2\end{aligned},$$

$$\mathbf{K}_{24}=-\Omega^2\int_{-h/2}^{h/2}\rho_p\mathrm{d}z_2\int_{-a-2r_b}^0\int_{-b/2}^{b/2}\boldsymbol{\Phi}_b^{\mathrm{T}}\big|_{x_1=d}\boldsymbol{\Psi}_p\mathrm{d}x_2\mathrm{d}y_2-\Omega^2\int_{-h/2}^{h/2}\rho_p\mathrm{d}z_2\int_{-a-2r_b}^0\int_{-b/2}^{b/2}\boldsymbol{\Phi}_b'^{\mathrm{T}}\big|_{x_1=d}x_2\boldsymbol{\Psi}_p\mathrm{d}x_2\mathrm{d}y_2,$$

$$\mathbf{K}_{42}=-\Omega^2\int_{-h/2}^{h/2}\rho_p\mathrm{d}z_2\int_{-a-2r_b}^0\int_{-b/2}^{b/2}\boldsymbol{\Psi}_p^{\mathrm{T}}\boldsymbol{\Phi}_b\big|_{x_1=d}\mathrm{d}x_2\mathrm{d}y_2-\Omega^2\int_{-h/2}^{h/2}\rho_p\mathrm{d}z_2\int_{-a-2r_b}^0\int_{-b/2}^{b/2}x_2\boldsymbol{\Psi}_p^{\mathrm{T}}\boldsymbol{\Phi}_b'\big|_{x_1=d}\mathrm{d}x_2\mathrm{d}y_2,$$

$$\begin{aligned}\mathbf{K}_{44}=&\int_{-h/2}^{h/2}\frac{z_2^2E_p}{1-\mu_p^2}\mathrm{d}z_2\int_{-a-2r_b}^0\int_{-b/2}^{b/2}\boldsymbol{\Psi}_{pxx}''^{\mathrm{T}}\boldsymbol{\Psi}_{pxx}''\mathrm{d}x_2\mathrm{d}y_2+\int_{-h/2}^{h/2}\frac{z_2^2E_p}{1-\mu_p^2}\mathrm{d}z_2\int_{-a-2r_b}^0\int_{-b/2}^{b/2}\boldsymbol{\Psi}_{pyy}''^{\mathrm{T}}\boldsymbol{\Psi}_{pyy}''\mathrm{d}x_2\mathrm{d}y_2\\&+\int_{-h/2}^{h/2}\frac{z_2^2E_p\mu_p}{1-\mu_p^2}\mathrm{d}z_2\int_{-a-2r_b}^0\int_{-b/2}^{b/2}\boldsymbol{\Psi}_{pyy}''^{\mathrm{T}}\boldsymbol{\Psi}_{pxx}''\mathrm{d}x_2\mathrm{d}y_2+\int_{-h/2}^{h/2}\frac{z_2^2E_p\mu_p}{1-\mu_p^2}\mathrm{d}z_2\int_{-a-2r_b}^0\int_{-b/2}^{b/2}\boldsymbol{\Psi}_{pxx}''^{\mathrm{T}}\boldsymbol{\Psi}_{pyy}''\mathrm{d}x_2\mathrm{d}y_2\\&+2\int_{-h/2}^{h/2}\frac{z_2^2E_p}{1+\mu_p}\mathrm{d}z_2\int_{-a-2r_b}^0\int_{-b/2}^{b/2}\boldsymbol{\Psi}_{pxy}''^{\mathrm{T}}\boldsymbol{\Psi}_{pxy}''\mathrm{d}x_2\mathrm{d}y_2+\frac{\Omega^2}{2}\int_{-h/2}^{h/2}\rho_B\mathrm{d}z_2\int_{-a-2r_b}^0\int_{-b/2}^{b/2}\left[\left(a^2-y_2^2\right)\boldsymbol{\Psi}_{pyy}''^{\mathrm{T}}\boldsymbol{\Psi}_{pyy}''\right]\mathrm{d}x_2\mathrm{d}y_2\end{aligned}.$$

References

1. W.L. Yang, D. He, Free vibration and buckling analyses of a size-dependent axially functionally graded beam incorporating transverse shear deformation, Results in physics 7 (2017) 3251-3263.
2. M.F. Chen, H.L. Chen, X.L. Ma, G.Y. Jin, T.G. Ye, Y.T. Zhang, Z.G. Liu. The isogeometric free vibration and transient response of functionally graded piezoelectric curved beam with elastic restraints, Results in physics 11 (2018) 712-725.
3. Y.Q. Wang, Y.F. Liu, Free vibration and buckling of polymeric shells reinforced with 3D graphene foams, Results in physics 14 (2019) 102510.
4. W. Zhang, Y. Niu, K. Behdinan, Vibration characteristics of rotating pretwisted composite tapered blade with graphene coating layers, Aerospace Science and Technology 98 (2020) 105644.

5. H. Rostami, F. Bakhtiari-Nejad, Modeling and dynamic study of rotating blades with adjustable stagger angle, Applied Mathematical Modelling 89 (2) (2021) 1599-1626.
6. R. Maretic, Vibration and stability of rotating plates with elastic edge supports, Journal of Sound and Vibration 210 (2) (1998) 291-294.
7. T.Y. Zhao, L.P. Jiang, H.G. Pan, J. Yang, S. Kitipornchai. Coupled free vibration of a functionally graded pre-twisted blade-shaft system reinforced with graphene nanoplatelets, Composite Structures 263 (2021) 113362.
8. T.Y. Zhao, Y.S. Cui, H.G. Pan, H.Q. Yuan, J. Yang. Free vibration analysis of a functionally graded graphene nanoplatelet reinforced disk-shaft assembly with whirl motion, International Journal of Mechanical Sciences 197 (2021) 106335.
9. R.M.R. Reddy, W. Karunasena, W. Lokuge, Free vibration of functionally graded GPL reinforced composite plates with different boundary conditions, Aerospace Science and Technology 78 (2018) 147-156.
10. H.H. Yoo, C. Pierre, Modal characteristic of a rotating rectangular cantilever plate, Journal Sound and Vibration 259 (1) (2003) 81-96.
11. L.J. Liu, Z.Y. Zhang, H.X. Hua, Dynamic characteristics of rotating cantilever plates with active constrained layer damping treatments, Smart Materials and Structures 16 (5) (2007) 1849-1856.
12. S.H. Hashemi, S. Farhadi, S. Carra, Free vibration analysis of rotating thick plates, Journal of Sound and Vibration 323 (1-2) (2009) 366-384.
13. L. Li, D.G. Zhang, Free vibration analysis of rotating functionally graded rectangular plates, Composite Structures 136 (2016) 493-504.
14. A.B. Arumugam, V. Rajamohan, Vibration analysis of rotating delaminated non-uniform composite plates, Aerospace Science and Technology 60 (2017) 172-182.
15. H. Rostami, F. Bakhtiari-Nejad, A.R. Ranji, Vibration of the rotating rectangular orthotropic Mindlin plates with an arbitrary stagger angle, Journal of Vibration and Control 25 (6) (2019) 1194-1209.
16. M.A. Rafiee, J. Rafiee, Z. Wang, H.H. Song, Z.Z. Yu, N. Koratkar, Enhanced mechanical properties of nanocomposites at low graphene content. ACS Nano. 3 (2009) 3884-3890.
17. A. Bidzard, P. Malekzadeh, S.R. Mohepour, Vibration of multilayer FG-GPLRC toroidal panels with elastically restrained against rotation edges, Thin-Walled Structures 143 (2019) 106209.
18. R. Gholami, R. Ansari, Nonlinear stability and vibration of pre/post-buckled multilayer FG-GPLRPC rectangular plates, Applied Mathematical Modelling 65 (2019) 627-660.

19. M. Arefi, E.M.R. Bidgoli, R. Dimitri, F. Tornabene, Free vibrations of functionally graded polymer composite nanoplates reinforced with graphene nanoplatelets, Aerospace Science and Technology 81 (2018) 108-117.
20. Y. Wang, C. Feng, C. Santiuste, Z. Zhao, J. Yang, Buckling and postbuckling of dielectric composite beam reinforced with Graphene Platelets (GPLs), Aerospace Science and Technology 91 (2019) 208-218.
21. K. Huang, H.L. Guo, Z.H. Qin, S.Q. Cao, Y.S. Chen, Flutter analysis of laminated composite quadrilateral plates reinforced with graphene nanoplatelets using the element-free IMLS-Ritz method, Aerospace Science and Technology 103 (2020) 105915.
22. H. Liu, H. Wu, Z. Lyu, Nonlinear resonance of FG multilayer beam-type nanocomposites: Effects of graphene nanoplatelet-reinforcement and geometric imperfection, Aerospace Science and Technology 98 (2020) 105702.
23. Y.Q. Wang, J.W. Zu, Vibration behaviors of functionally graded rectangular plates with porosities and moving in thermal environment, Aerospace Science and Technology 69 (2017) 550-562.
24. D. Shahgholian, M. Safarpour, A.R. Rahimi, A. Alibeigloo, Buckling analyses of functionally graded graphene-reinforced porous cylindrical shell using the Rayleigh-Ritz method, Acta Mechanica 231 (5) (2020) 1887-1902.
25. C. Tao, T. Dai, Isogeometric analysis for postbuckling of sandwich cylindrical shell panels with graphene platelet reinforced functionally graded porous core, Composite Structures 6 (2020) 113258.
26. D. Chen, J. Yang, S. Kitipornchai, Nonlinear vibration and postbuckling of functionally graded graphene reinforced porous nanocomposite beams, Composites Science and Technology 142 (12) (2017) 235-245.
27. J. Yang, D. Chen, S. Kitipornchai, Buckling and free vibration analyses of functionally graded graphene reinforced porous nanocomposite plates based on Chebyshev-Ritz method, Composite Structures 193 (1) (2018) 281-294.
28. K. Gao, W. Gao, D. Chen, J. Yang, Nonlinear free vibration of functionally graded graphene platelets reinforced porous nanocomposite plates resting on elastic foundation, Composite Structures 204 (2018) 831-846.
29. Y.H. Dong, B. Zhu, Y. Wang, L.W. He, Y.H. Li, J. Yang, Analytical prediction of the impact response of graphene reinforced spinning cylindrical shells under axial and thermal loads, Applied Mathematical Modelling 71 (2019) 331-348.
30. S.Y. Zhao, Z.C. Yang, S. Kitipornchai, J. Yang, Dynamic instability of functionally graded

porous arches reinforced by graphene platelets, Thin-Walled Structures 147 (2020) 106491.

31. Y.Q. Wang, C. Ye, J.W. Zu, Nonlinear vibration of metal foam cylindrical shells reinforced with graphene platelets, Aerospace Science and Technology 85 (2019) 359-370.
32. B. Anirudh, M. Ganapathi, C. Anant, O. Polit, A comprehensive analysis of porous graphene-reinforced curved beams by finite element approach using higher-order structural theory: Bending, vibration and buckling, Composite Structures 222 (2019) 110899.
33. S.S. Mirjavadi, M. Forsat, A. Hamouda, M.R. Barati, Dynamic response of functionally graded graphene nanoplatelet reinforced shells with porosity distributions under transverse dynamic loads, Materials Research Express 6 (7) (2019) 075045
34. D.A. Narayan, T. Ben Zineb, O. Polit, B. Pradyumna, M. Ganapathi, Large amplitude free flexural vibrations of functionally graded graphene platelets reinforced porous composite curved beams using finite element based on trigonometric shear deformation theory, International Journal of Non-Linear Mechanics 116 (2019) 302-317.
35. K. Asemi, M. Babaei, F. Kiarasi, Static, natural frequency and dynamic analyses of functionally graded porous annular sector plates reinforced by graphene platelets, Mechanics Based Design of Structures and Machines (2020) 1822865.
36. N.V. Nguyen, H. Nguyen-Xuan, D. Lee, J. Lee, A novel computational approach to functionally graded porous plates with graphene platelets reinforcement, Thin-Walled Structures 150 (2020) 106684
37. S. Kitipornchai, D. Chen, J. Yang, Free vibration and elastic buckling of functionally graded porous beams reinforced by graphene platelets, Materials and Design 116 (15) (2017) 656-665.
38. C. Feng, S. Kitipornchai, J. Yang, Nonlinear free vibration of functionally graded polymer composite beams reinforced with graphene nanoplatelets (GPLs), Engineering Structures 140 (1) (2017) 110-119.